ESTIMATION OF VELOCITY IN UNDERWATER WIRELESS CHANNELS

A Thesis
Presented to
The Academic Faculty

by

Bryan S. Blankenagel

In Partial Fulfillment
of the Requirements for the Degree
Master of Science in the
School of Electrical and Computer Engineering

Georgia Institute of Technology
December 2013

ESTIMATION OF VELOCITY IN UNDERWATER WIRELESS CHANNELS

Approved by:

Professor Alenka Zajic, Advisor
School of Electrical and Computer Engineering
Georgia Institute of Technology

Professor Ghassan AlRegib
School of Electrical and Computer Engineering
Georgia Institute of Technology

Professor Biing Hwang Juang
School of Electrical and Computer Engineering
Georgia Institute of Technology

Date Approved: 15 November 2013

To Nikki,

one of my best friends,

who helped to get me through it all.

ACKNOWLEDGEMENTS

I want to thank my advisor, Prof. Alenka Zajic, for her support and dedication to my research. Without her continued interest in my development as a student and researcher, this thesis would not have been possible.

I also want to thank my committee members for their instruction and contributions to the improvement of this thesis.

TABLE OF CONTENTS

LIST OF FIGURES

SUMMARY

Underwater communication is necessary for a variety of applications, including transmission of diver speech, communication between manned and/or unmanned underwater vehicles, and data harvesting for environmental monitoring, to name a few. Examples of communication between underwater vehicles include unmanned or autonomous underwater vehicles (UUV or AUV) for deep water construction, military UUVs such as submarine drones, repair vehicles for deep water oil wells, scientific or resource exploration, etc. Examples of underwater communication between fixed submerged devices are sensor networks deployed on the ocean floor for seismic monitoring and tsunami prediction, pollution monitoring, tactical surveillance, analysis of resource deposits, oceanographic studies, etc.

The underwater communication environment is a challenging one. Radio signals experience drastic attenuation, while optical signals suffer from dispersion. Because of these issues, acoustic (sound) signals are usually used for underwater communication. Unfortunately, acoustics has its own problems, including limited bandwidth, slow propagation, and signal distortion. Some of these limitations can be overcome with advanced modulation and coding, but to do so requires better understanding of the underwater acoustic propagation environment, which is significantly different than air- or space-based radio propagation. The underwater environment must be studied and characterized to exploit these advanced modulation and coding techniques.

This thesis addresses some of these concerns by proposing a derivation of the envelope level crossing rate of the underwater channel, as well as a simulation model for the channel, both of which agree well with the measured results. A velocity

estimator is also proposed, but suffers from a high degree of root mean square error.

CHAPTER I

INTRODUCTION

1.1 Motivation

Underwater communications are used for a variety of applications, particularly in the defense and scientific communities. Some examples of communications between underwater vehicles are Unmanned or Autonomous Underwater Vehicles (UUV or AUV), used for deep water construction as well as repairs of deep water oil wells, exploration for resources or other scientific endeavors, communication between submarines, etc. Other examples of underwater communication include data harvesting for environmental monitoring, transmission of diver speech, tactical surveillance, assisted navigation, pollution monitoring, etc. From the communications perspective, the ultimate goal is to create an underwater network that consists of distributed underwater sensors nodes and underwater vehicles that perform collaborative monitoring and communication as illustrated in Fig. 1.1. Unfortunately, underwater communication is an extremely complicated and challenging problem. Use of wires or cables hampers the potential applications, or makes them completely unfeasible. Existing wireless communication solutions are also problematic, with issues such as low data rates, limited range of effectiveness, and low energy efficiency. The main reason for this poor performance is that the underwater environment is ill suited for traditional wireless communication methods. Radio signals are severely attenuated due to seawater being a good conductor, and can remain operative within a range of only a few meters. Optical communications also have a very short range, mainly because of dispersion from murkiness or particles in the water.

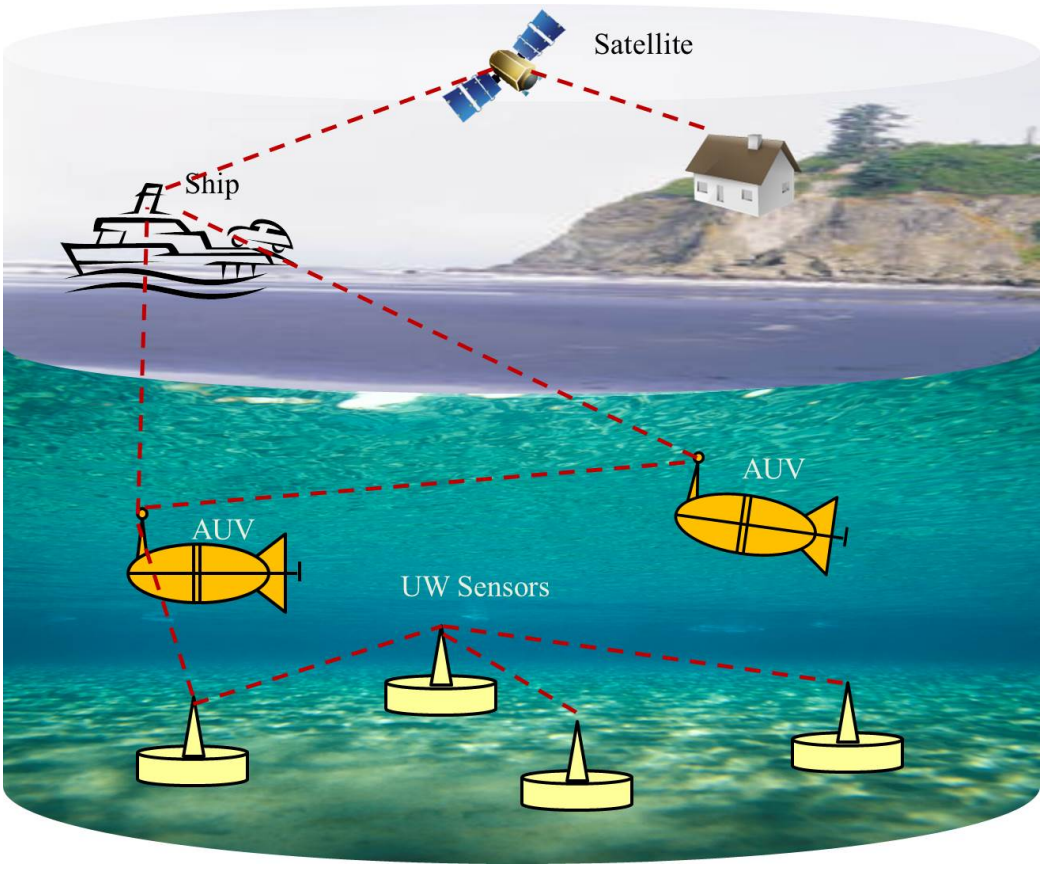

Figure 1.1: An acoustic network of underwater sensors and autonomous underwater vehicles.

Underwater wireless communication mostly uses acoustics (sound) to mitigate the range problem, as acoustic waves can travel long distances in water. However, acoustic communication has drawbacks as well, including propagation speed that is orders of magnitude slower than radio or optics, an operating spectrum limited to kilohertz instead of gigahertz, and many sources of signal distortion that reduce achievable data rates. Recent advances in modulation and coding techniques have demonstrated their capabilities in greatly enhancing the data rate in radio communication However, the differences between the underwater propagation environment and the air- and space-based radio environment must be taken into account in order to exploit these advanced modulations and coding.

1.2 Research Contributions

This section briefly summarizes the contributions of the thesis.

- Derivation of envelope level crossing rate for underwater mobile-to-mobile channels and comparison with measured data. [27].
- Development of a new sum-of-sinusoids based simulation model for underwater mobile-to-mobile channels [28].
- Development of a velocity estimator for underwater mobile-to-mobile channels.

1.3 Thesis Outline

The remainder of the thesis is organized as follows. Chapters 2 contains a background of the underwater propagation environment and noise, and covers several acoustic propagation principles. Chapter 3 contains descriptions of previous research into the statistical properties of the underwater acoustic channel. It includes geometric depictions of the channel, describing the important parameters that are used for calculations of the various statistical characteristics. Chapter 4 begins the research contributions of this thesis, describing the derivation of the level crossing rate of the underwater channel, drawing from the statistical properties of chapter 3. Chapter 5 describes the development of a simulator for the acoustic fading channel of interest. Chapter 6 describes how to estimate the velocity of the transmitter and receiver in the underwater environment, using the level crossing rate and the simulator described in chapters 4 and 5, respectively. Finally, chapter 7 concludes the thesis by summarizing the research contributions, as well as suggesting future research possibilities in the field.

CHAPTER II

BACKGROUND

The underwater environment is rather hostile towards electromagnetic and optical communications. The conductivity of seawater means that electromagnetic waves can only propagate any significant distance at extremely low frequencies, such as 30-300Hz. Transmission at these frequencies requires very large antennas and high transmission power. Optical waves do not experience this same level of attenuation, but face a different problem in scattering. Because of these issues, underwater communications primarily relies on acoustic (pressure) waves [1].
The underwater acoustic (UWA) channel remains one of the most challenging wireless communication environments due to several issues:

- Acoustic waves travel through water at a low speed (1500 m/s), which is five orders of magnitude slower than radio waves. This low propagation speed significantly increases the latency in the communication system.

- Underwater acoustic propagation is characterized by significant frequency-dependent attenuation. Spreading loss, absorption loss, and scattering loss are three of the primary factors that attenuate underwater acoustic signals.

- The available bandwidth of an UWA channel critically depends on the transmission loss. This loss increases with both range and frequency, and severely limits the bandwidth available [2], [3]. As an example, long-range systems working over several tens of *kilometers* may have only a few kHz of bandwidth, while short-range systems operating over several tens of *meters*

may have one to a few hundred kHz of bandwidth [4].

- Acoustic signals are strongly influenced by speed of sound variations at different water depths and temperatures, by reflections from the ocean surface and ocean floor, and by the locations of the transmitter and receiver. As a result, a received signal is impacted by time-varying multipath, which may result in inter-symbol interference and Doppler spreads. Propagation speed variation is a crucial factor in acoustic channels. This impact is much more severe than in radio channels, especially in shallow water channels [2].

These factors together produce a communication medium that blends the worst parts of traditional radio propagation environments: poor link quality of a terrestrial system and high latency of a satellite system. Making the problem even more difficult, there is no "typical" underwater acoustic environment, so there is no "typical" underwater acoustic communication channel. Different physical processes pose significant problems to reliable communications in different environments, resulting in different challenges to a system. Therefore, a system that works effectively in one environment, for example, a shallow water environment, may fail completely in another environment such as a deep water environment. The design of reliable general purpose systems that work effectively across many ocean environments is an open problem.

2.1 An Underwater Communication System

A simple schematic of an underwater communication scheme, involving a projector (transmitter) and a hydrophone (receiver), is presented in Fig. 2.1. The projector receives the data input and produces modulated signals. These modulated signals are then amplified to a sufficient level for successful reception and converted from the electrical to acoustical signals. On the receiver side, the sensitivity of the hydrophone converts the sound pressure that reaches the hydrophone to electrical

energy. This signal is then detected, amplified and demodulated at the receiver.

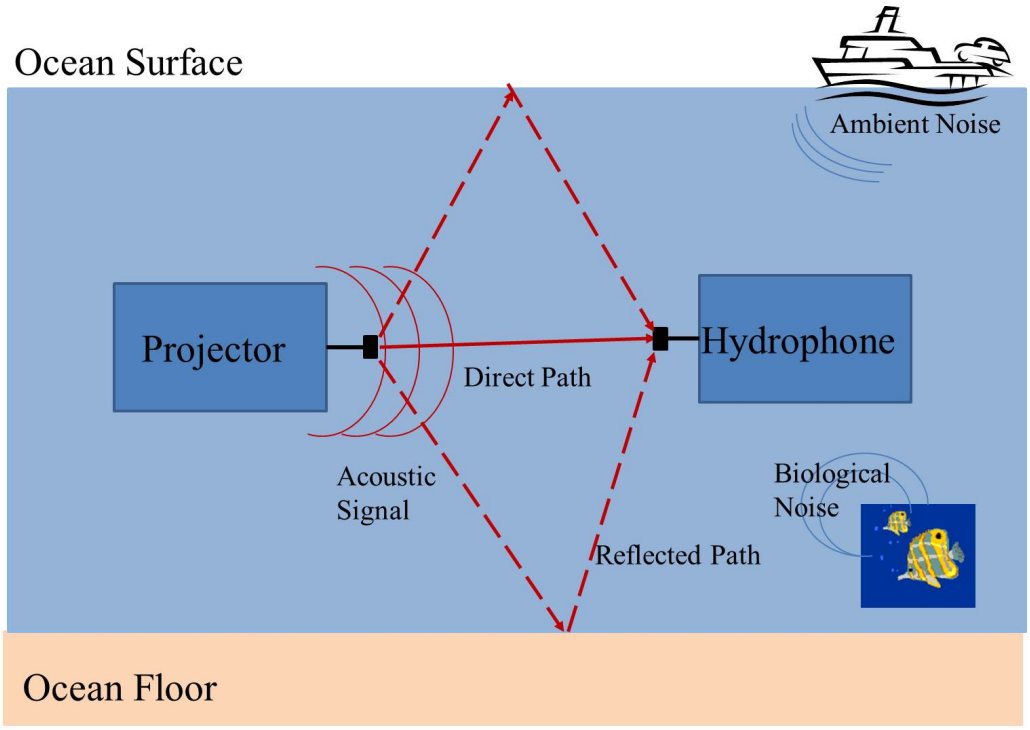

Figure 2.1: A simple schematic of an underwater communication scheme.

2.2 Underwater Noise

Underwater communication is impacted by frequency-dependent noise, consists of *ambient noise* and *site-specific noise*.

Ambient noise is always present in the background of a quiet deep sea and comes from such sources as turbulence, breaking waves, rain, distant shipping, etc.

Conversely, site-specific noise is present only at certain locations. For example, ice cracking in polar regions or snapping shrimp in warmer waters create site-specific acoustic noise.

The noise level contains a significant amount of information concerning the state of the ocean surface, the atmosphere over the ocean, tectonic processes in the earth's crust under the ocean, the behavior of marine animals, etc. The total noise level in

dB can be written as [6]

$$\begin{aligned} N(f, v_s, S, v_w) &= N_{\text{traffic}}(f) + N_{\text{turb}}(f) + N_{\text{vessel}}(f, v_s) \\ &+ N_{\text{bio}}(f, SL) + N_{\text{ss}}(f, v_w) + N_{\text{term}}(f), \end{aligned} \tag{2.1}$$

where f is the frequency in kHz, and

- $N_{\text{traffic}}(f)$ [dB] is the shipping noise (traffic) at$10 - 300$ Hz and can be expressed as

$$N_{\text{traffic}}(f) = 10 \cdot \log_{10}\left(\frac{3 \cdot 10^8}{1 + 10^4 \cdot f^4}\right); \tag{2.2}$$

- $N_{\text{turb}}(f)$ [dB] is the turbulence noise and can be expressed as

$$N_{\text{turb}}(f) = 30 - 30 \cdot \log_{10}(f); \tag{2.3}$$

- $N_{\text{vessel}}(f, v_s)$ [dB] is the noise of a vessel, a function of frequency f and vessel speed v_s, and is usually experimentally determined;

- $N_{\text{bio}}(f, SL)$ [dB] is the biological noise (fishes, shrimps, etc.), a function of frequency f and season-location SL, and its level is usually experimentally determined.

- $N_{\text{ss}}(f, v_w)$ is the sea state noise, which depends on frequency f [kHz] and wind speed v_w [kn], and can be expressed as

$$N_{\text{ss}}(f, v_w) = 40 + 10 \cdot \log_{10}\left(\frac{v_w^2}{1 + f^{5/3}}\right). \tag{2.4}$$

- $N_{\text{term}}(f)$ is the thermal noise and occurs due to molecular agitation (Brownian Motion). Thermal noise is a function of frequency f [kHz] and can be expressed as

$$N_{\text{term}}(f) = -15 + 20 \cdot \log_{10}(f). \tag{2.5}$$

The main sources of noise at low frequencies ($0.1 - 10$ Hz) are earthquakes, underwater volcanic eruptions, distant storms, turbulence in the ocean and atmosphere, etc. In the $50 - 300$ Hz frequency band, distant ship traffic is the main cause of underwater noise. In the $0.5 - 50$ kHz frequency band, underwater noise is directly associated with the state of the ocean surface and the wind in the immediate area. Thermal noise dominates at frequencies above 100 kHz.
When simulating communication systems, ambient noise is often approximated as Gaussian, but not white. Unlike ambient noise, site-specific noise often contains significant non-Gaussian components, so it cannot be modelled as Gaussian noise.

2.3 Propagation Principles

Acoustic waves propagate from the transmitter to the receiver (hydrophone) by four main propagation methods: *direct propagation*, *refraction*, *reflection*, and *scattering*. Direct propagation occurs when sound energy from the transmitter makes its way to the receiver directly along a line of sight (LoS) path. Refraction occurs because of spatial variability of the speed of sound, as described in 2.4. Finally, reflection and scattering are created by sound waves interacting with the surface, bottom, or other objects in the channel, such as fish. The incoming acoustic waves are a superposition of the wave coming from the LoS path and all the waves coming from other directions due to refraction, reflection, and scattering. This effect is known as *multipath propagation*, and is similar in its effects to, but much more pronounced than, multipath propagation in radio channels.

2.4 Refraction

The refraction of sound in the ocean happens because of spatial variability of the speed of sound. When a sound wave propagating in a medium with speed of sound c_1 encounters another medium having different speed of sound c_2, the sound wave changes its direction, as shown in Fig. 2.2. Variations of the sound velocity c in the

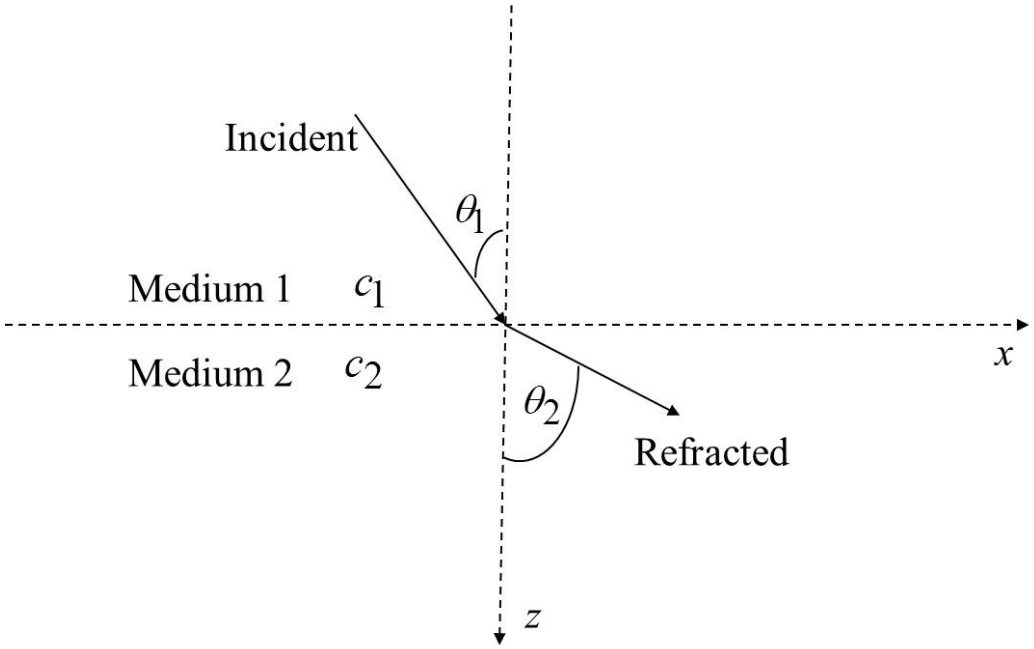

Figure 2.2: Refraction at two different interfaces.

ocean are relatively small, i.e., c lies between 1450 m/s and 1540 m/s. Even such small changes of c can, however, still result in significant refraction effects. Numerous laboratory and field measurements have shown that the sound speed increases with temperature T [5], hydrostatic pressure P (or depth z), and the salinity S. An empirical formula for the speed of sound is [6]

$$\begin{aligned} c &= 1449.2 + 4.6 \cdot T - 0.055 \cdot T^2 + 0.00029 \cdot T^3 \\ &+ 1.34 - 0.01 \cdot T)(S - 35) + 0.016 \cdot z, \end{aligned} \tag{2.6}$$

where temperature T is expressed in $^\circ C$, salinity S in percentiles, depth z in meters, and sound velocity c in m/s. Equation (2.6) is valid for $0^\circ C \leq T \leq 35^\circ C$, $0 \leq S \leq 45\%$, and $0 \leq z \leq 1000$ m.

2.4.1 Typical Vertical Profiles of Sound Velocity and Corresponding Conditions of Sound Propagation

Sound velocity varies with temperature, salinity and depth, as noted in Section 2.4. The sound velocity profile $c(z, T(z), S(z))$ and the distribution of the sound velocity

gradient with depth are two of the most important parameters for determining the sound propagation type in the ocean. For one type of profile $c(z, T(z), S(z))$, sound can propagate hundreds of kilometers, whereas for another type, sound at the same frequency can propagate only a few tens of kilometers, or even less.

The $c(z, T(z), S(z))$ profiles are different in various parts of the ocean, and also vary with time. The greatest fluctuations occur in the upper ocean, mostly due to seasonal variations in temperature and salinity. For ocean depths smaller than 200 m, the dominant factor that impacts the velocity of sound is the temperature. Between 200 m and 400 m, both temperature and depth have a significant impact on the velocity of sound. At ocean depths greater than 400 m, the sound velocity almost purely depends on the depth. The velocity of sound also depends on salinity S. As S increases, c also increases, but the shape of the speed-of-sound profile remains unchanged.

Next, four main forms of the sound-velocity profile and the corresponding acoustic channel types are described: underwater sound channel, surface sound channel, anti-waveguide sound channel, and shallow water sound channel.

2.4.2 Underwater Sound Channel

The typical sound velocity profile in deep-water areas is characterized by the existence of a minimum sound velocity at a certain depth z_m, as shown in Fig. 2.3 (a). The depth z_m is shown as an axis of the underwater sound channel. Above this axis, the sound velocity increases mainly due to temperature increase. The sound velocity increases mainly due to hydrostatic pressure below the axis. If a sound source is located on the axis of the underwater sound channel or near it, some part of the sound energy is trapped in the underwater sound channel because of refraction (i.e., refraction bends the sound waves back toward the axis). The sound then propagates within the channel, not reaching the bottom or surface, and

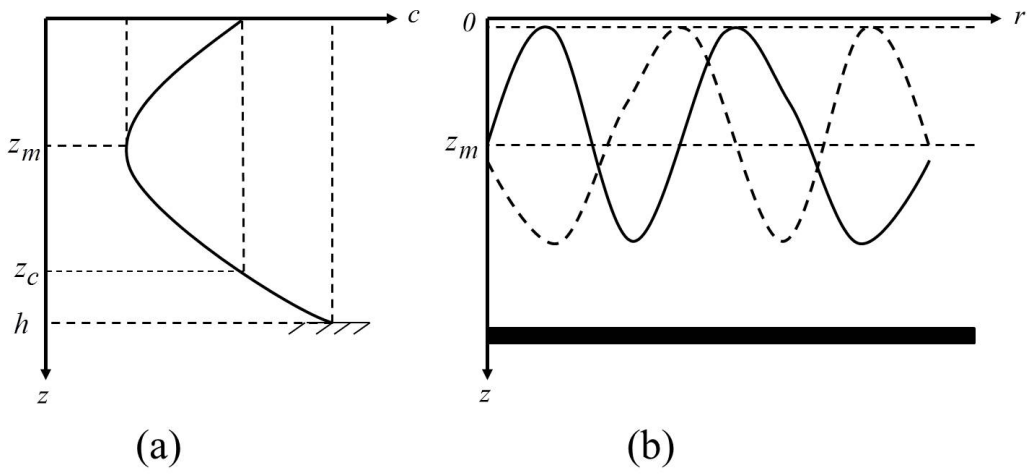

Figure 2.3: (a) Profile of an underwater sound channel of the first kind ($c_0 < c_h$); (b) Ray diagram of the underwater sound channel of the first kind.

therefore, does not undergo scattering and absorption at these boundaries [6]. Depending on the ratio of the sound velocity at the surface c_0 and the sound velocity at the bottom c_h, there are two types of underwater sound channels:

- When c_0 is smaller than c_h, the rays leaving the source at small or moderate grazing angles return to the channel axis repeatedly, propagating as if in a waveguide. This type of channel is called ***underwater sound channel of the first kind***.

  In this type of underwater sound channel, waveguide propagation can be observed in the interval depths of $0 \leq z \leq z_c$. The depths $z = 0$ and $z = z_c$ are the boundaries for the underwater sound channel. The channel traps all sound rays that leave the source (which is located on the underwater sound channel axis) at grazing angles $\chi < \chi_{\max}$, where

$$\chi_{\max} = \sqrt{\frac{2(c_0 - c_m)}{c_m}}, \tag{2.7}$$

  and c_m and c_0 are the sound velocities at the axis and boundaries of the channel, respectively. Hence, the greater the difference between c_0 and c_m, the

larger the interval of angles in which the rays are trapped, making the waveguide more effective.

- When c_0 is greater than c_h, the sound bounces between the bottom and the depth z_c, as shown in Fig. 2.4. This type of channel is called ***underwater sound channel of the second kind***. As shown in Fig. 2.4 (b), trapped rays do not propagate above the depth z_c.

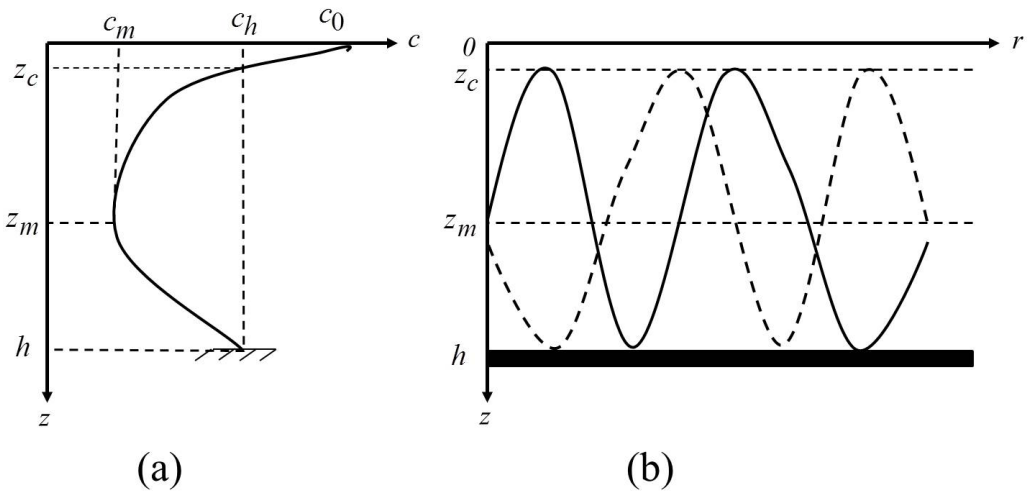

Figure 2.4: (a) Profile of an underwater sound channel of the second kind ($c_0 > c_h$); (b) Ray diagram of the underwater sound channel of the second kind.

2.4.3 Surface Sound Channel

A surface sound channel occurs when the axis is at the surface, or when $c_m = c_0$. A typical profile for this channel is shown in Fig. 2.5. The sound velocity increases with greater depth until $z = h$ and then begins to decrease, as shown in Fig. 2.5 (a). Rays leaving the source at grazing angles $\chi < \chi_b$ (where χ_b is the grazing angle of the boundary ray tangent to the lower boundary of the channel as shown in Fig. 2.5 (b)) propagate with multiple reflections from the surface [6]. If the ocean surface is smooth, these rays will remain in the sound channel no matter the distance from the source and give rise to waveguide propagation. However, if the ocean surface is

rough, part of the sound energy is scattered into angles $\chi > \chi_b$ at each contact with the surface and, therefore, will leave the sound channel. Because of this, the sound field decays in the sound channel, but its level increases in the area below the channel. This type of channel occurs where the temperature and salinity in the upper ocean layer are almost constant, typically in the tropical and moderate zones of the ocean.

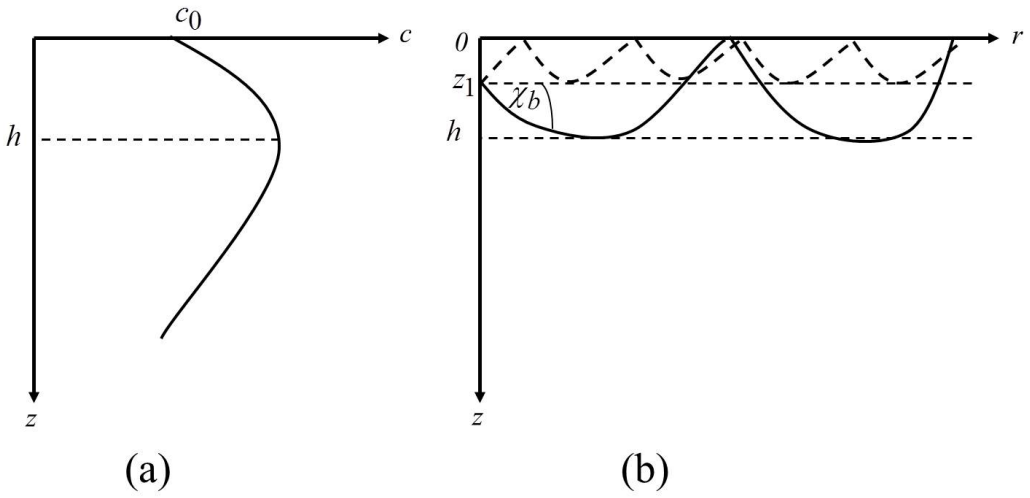

Figure 2.5: (a) Profile of a surface sound channel (b) Ray diagram of the surface sound channel.

2.4.4 Antiwaveguide Sound Channel

The antiwaveguide sound channel occurs when the sound velocity decreases monotonically with the depth as shown in Fig. 2.6 (a). Such sound velocity profiles are often a result of intensive heating of the upper ocean layer by solar radiation. From Fig. 2.6 (b) it can be observed that all rays refract downwards. The ray that is tangent to the surface is the one that will propagate farthest in this type of channel. For typical conditions in the ocean, the distance from the source to the shadow zone is only a few kilometers.

The shadow zone shown in Fig. 2.6 (b) is not a region of zero sound intensity. The sound energy will penetrate into the shadow zone due to diffraction, in the ideal

case. In reality, some sound waves reflected from the bottom and scattered by random inhomogeneities of the medium also produce sound in this zone.

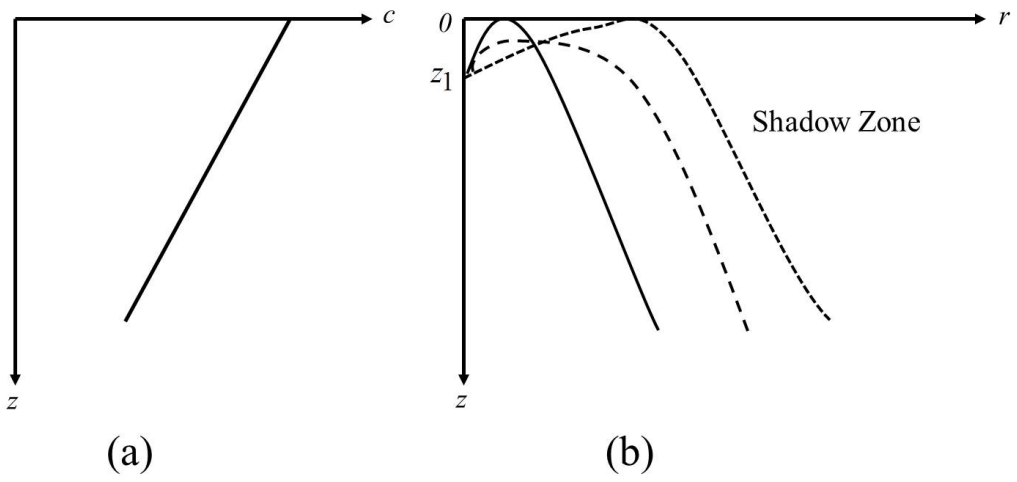

Figure 2.6: (a) Profile of an antiwaveguide sound channel (b) Ray diagram of the antiwaveguide sound channel.

2.4.5 Shallow Water Sound Channel

Propagation in a shallow water sound channel corresponds to the case when every ray emitted from the source, when continued long enough, is reflected from the bottom. A typical sound velocity profile for this case is shown in Fig. 2.7 (a) and the corresponding ray diagram is shown in Fig. 2.7 (b). This type of propagation is characteristic for shallow seas and the ocean shelves, especially during the summer-autumn period when the upper water layers are well heated. Propagation over large distances in this type of channel results in great loss of acoustic energy because every reflection from the bottom significantly attenuates the sound waves.

2.5 Reflection

Reflection occurs when a sound wave propagating in one medium, such as water, is incident upon another medium having different properties, such as air or ground. The sound wave is then divided between a reflected component and a transmitted

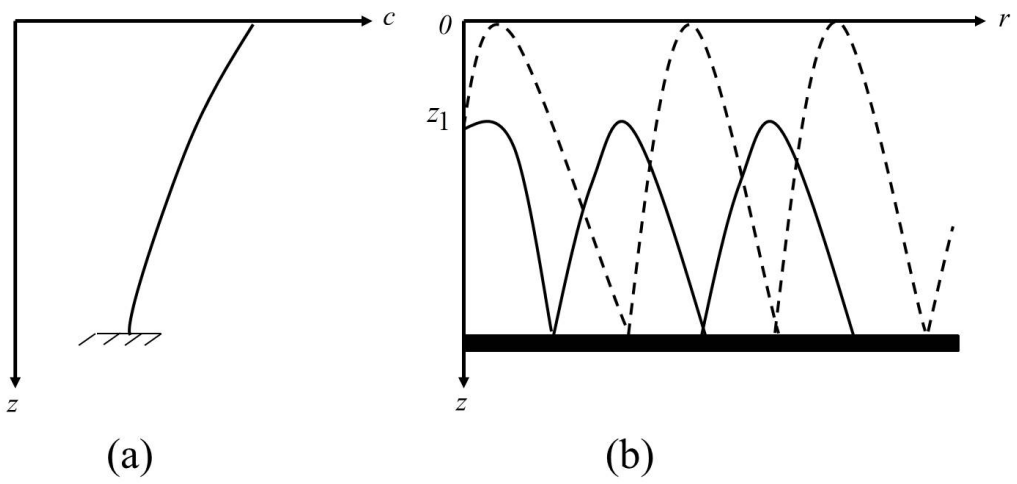

Figure 2.7: (a) Profile of a shallow water sound channel (b) Ray diagram of the shallow water sound channel.

(continuing) component, as shown in Fig. 2.8.

The surface and bottom of the ocean are highly complex boundaries. They are usually rough, and the ground underwater is usually considered an inhomogeneous medium. In order to analytically obtain the reflection coefficient, the surface and bottom can roughly be approximated as flat surfaces. This allows them to be modeled as reflective surfaces with specular reflection. The simplest case of plane waves will here be considered.

Figure 2.8 shows reflection at the interface separating two homogeneous fluid media with densities ρ_i and sound speeds c_i, for $i = 1, 2$. The incident angles in the $x - z$ plane are denoted by θ_i, for $i = 1, 2$. Assuming that the incident wave has the unit amplitude, and denoting the amplitudes of the reflected and the transmitted waves as R and T, respectively, the acoustic pressures can be written as [6]

$$p_i = \exp(jk_1(x\sin\theta_1 + z\cos\theta_1) - j2\pi ft), \tag{2.8}$$

$$p_r = R\exp(jk_1(x\sin\theta_1 - z\cos\theta_1) - j2\pi ft), \tag{2.9}$$

$$p_t = T\exp(jk_2(x\sin\theta_2 + z\cos\theta_2) - j2\pi ft), \tag{2.10}$$

where $k_1 = 2\pi f/c_1$ and $k_2 = 2\pi f/c_2$. In the subsequent equations, the common time

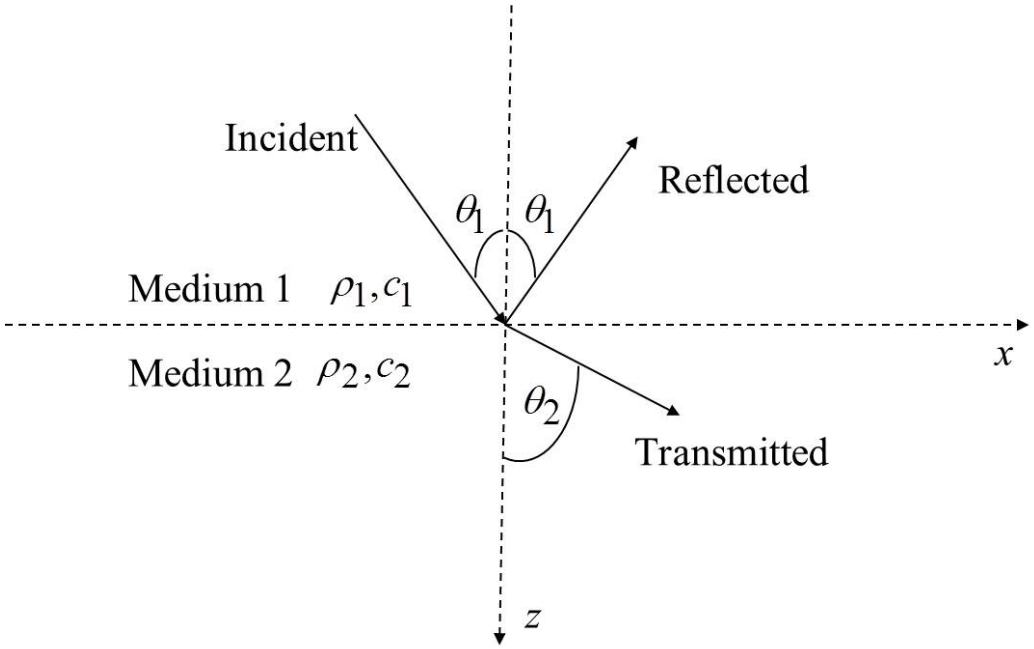

Figure 2.8: Reflection and transmission at two different interfaces.

factor $\exp(-j2\pi ft)$ is omitted for brevity.

The quantities R, T, and θ_2 are determined from the boundary conditions that require continuity of pressure and vertical particle velocity at the interface $z = 0$. With the total pressure in medium 1 given by $p_1 = p_i + p_r$ and the pressure in medium 2 by $p_2 = p_t$, the boundary conditions can be written as

$$p_1 = p_2, \tag{2.11}$$

$$\frac{1}{j2\pi f\rho_1}\frac{dp_1}{dz} = \frac{1}{j2\pi f\rho_2}\frac{dp_2}{dz}, \tag{2.12}$$

where d/dz denotes the first derivative with respect to z. It can be shown that the requirement of continuity of pressure and vertical particle velocity at $z = 0$ leads to

$$1 + R = T\exp(j(k_2\cos\theta_2 - k_1\cos\theta_1)x), \tag{2.13}$$

$$\frac{k_1}{\rho_1}(1 - R)\cos\theta_1 = \frac{k_2}{\rho_2}T\cos\theta_2. \tag{2.14}$$

Since the left side is independent of x, this becomes *Snell's law of refraction*:

$$k_1 \cos\theta_1 = k_2 \cos\theta_2, \tag{2.15}$$

$$\frac{\sin\theta_1}{\sin\theta_2} = \frac{k_1}{k_2} = \frac{c_1}{c_2} = n. \tag{2.16}$$

This law states that the horizontal component of the wave vector does not vary across the interface. From equations (2.13) and (2.15),

$$1 + R = T. \tag{2.17}$$

From (2.16),

$$m(1 - R)\cos\theta_1 = nT\cos\theta_2, \tag{2.18}$$

where $m = \rho_2/\rho_1$. From (2.17) and (2.18), the reflection and transmission coefficients R and T can be written, respectively, as

$$R = \frac{m\cos\theta_1 - n\cos\theta_2}{m\cos\theta_1 + n\cos\theta_2} = \frac{m\cos\theta_1 - \sqrt{n^2 - \sin^2\theta_1}}{m\cos\theta_1 + \sqrt{n^2 - \sin^2\theta_1}}, \tag{2.19}$$

$$T = \frac{2m\cos\theta_1}{m\cos\theta_1 + n\cos\theta_2} = \frac{2m\cos\theta_1}{m\cos\theta_1 + \sqrt{n^2 - \sin^2\theta_1}}. \tag{2.20}$$

2.6 Scattering

A sound wave in water hitting a rough surface will create scattered waves. The scattered sound field will have coherent and incoherent components. The coherent component is a wave propagating in the direction of specular reflection and can be obtained from statistical averaging of the scattered field. The effect of scattering from a rough surface is often considered as additional loss to the specularly reflected (coherent) component, because the scattering of energy is away from the specular direction. If the ocean bottom or surface are modeled as surfaces with random roughness, and if the roughness is small compared to the acoustic wavelength, then the reflection loss can be considered to be modified in a simple fashion by the

scattering process. A formula often used to describe reflectivity from a rough boundary is

$$\hat{R}\theta) \quad = \quad R(\theta)e^{-0.5\Gamma^2}, \tag{2.21}$$

where $\hat{R}(\theta)$ is the new reflection coefficient, reduced because of scattering at the randomly rough interface. Γ is the Rayleigh roughness parameter defined as

$$\Gamma \quad = \quad 2k\sigma \sin\theta, \tag{2.22}$$

where $k = 2\pi/\lambda$, σ is the root mean square displacement of the rough surface, and θ is the grazing angle of the sound wave relative to the horizontal plane. For large values of the Rayleigh parameter ($\Gamma \gg 1$), the coherent component is close to zero, and the scattered field is almost completely incoherent.

CHAPTER III

STATISTICAL CHARACTERIZATION OF MULTIPATH PROPAGATION

3.1 Overview

Underwater sound propagation is described mathematically using the wave equation, whose boundary conditions and parameters describe the ocean environment. Of the five types of existing models that describe sound propagation in the ocean: fast field program, normal mode, parabolic equation, direct finite-difference (or finite element), and ray theory, ray theory is most often used in practice for modeling sound propagation [6].

In most locations and for the frequencies at which communication is possible, the ocean can be modeled as a waveguide with reflective surfaces and a sound speed that varies spatially. It is becoming more common to use ray tracing to determine the deterministic multipath structure for communication channel modeling [7], [8]. Random signal fluctuations (micro-multipaths) cause time variability in the channel response, and are associated with each deterministic propagation path (macro-multipath). In shallow water, the overall time variability is most strongly affected by surface scattering caused by waves. In deep water, internal waves also contribute to the time variation along each deterministic path of signal propagation. Some of these models can by modeled statistically [6].

In order to address the challenges in underwater communications, statistical characterization and modeling of the acoustic wireless communication channel is necessary. Although many statistical and deterministic channel models that characterize underwater sound propagation are in use [3], [7]-[11], a statistical

framework for these channels, i.e., correlation functions, power delay spectral density, Doppler power spectral density, level-crossing rate, etc., has only recently been addressed. These statistics are important for accurate and robust design of underwater communication systems. They are often used for determining propagation delay spread and available capacity, as well as investigation of spatial diversity. The closed form expressions for these statistics can also be utilized to estimate physical parameters of the channel, such as angle spread, mean angles of arrival/departure, etc. The following sections address the most recent results about statistical characterization of multipath propagation in UV-to-UV acoustic channels.

3.2 Received Envelope Distribution

A time-varying multipath communication channel is often modeled as a tapped delay line, with the tap spacing being equal to the reciprocal of twice the channel bandwidth, and the tap gains being modeled as stochastic processes with certain distributions and power spectral densities. RF radio channels are modeled by a number of different standardized and well-accepted probability distributions (e.g. Rayleigh fading) and power spectral densities of the fading process (e.g. the Jakes model). However, there is no consensus yet regarding statistical characterization of underwater acoustic communication channels. Some experimental results for a shallow-water medium-range channel suggest that the channel could be characterized as K-distributed fading [12], and others have suggested Rice or Rayleigh fading [11]. The deep water channel has been modeled as a Rayleigh fading channel, but experimental results are scarce.

3.3 Statistical Modeling of UV-to-UV Frequency Flat Acoustic Fading Channels

The first statistical characterizations of UV-to-UV acoustic channels are reported in [13]-[17]. A statistical model for time-invariant stationary shallow water acoustic

channels was first proposed by Abdi and Guo [13], considering only macro-multipath effects. A time-varying shallow water acoustic channel was later proposed [17], which accounts for both macro- and micro-multipath effects, and which will be detailed as follows.

The UV-to-UV acoustic channel in [17] is modeled as a two-dimensional (2-D) waveguide bounded on the top and the bottom by the ocean surface and floor. These boundaries reflect the acoustic signal, resulting in multiple macro-eigenrays traveling between transmitter (T_x) and receiver (R_x), as shown in Fig. 3.1.

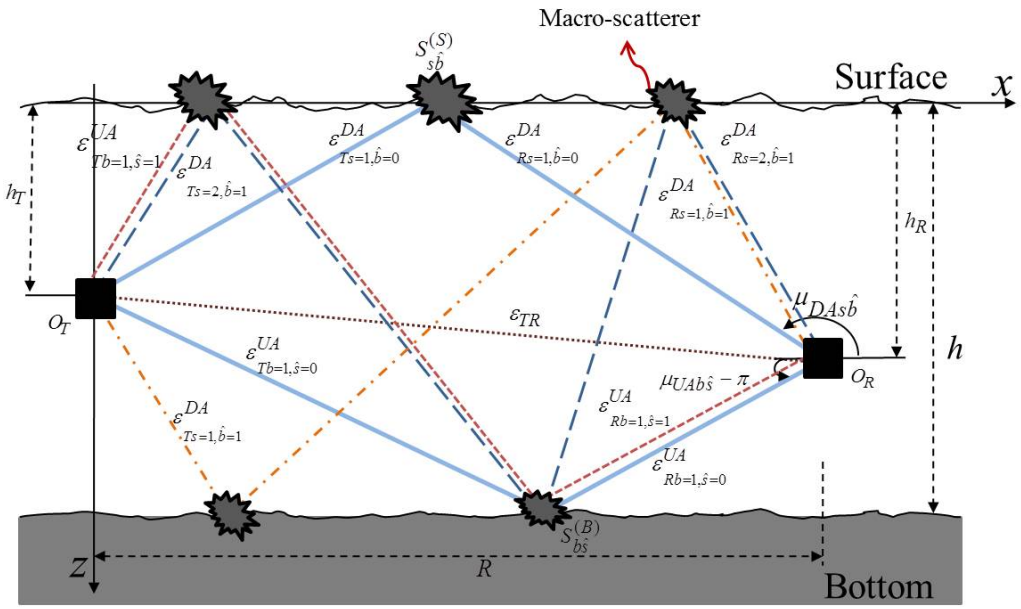

Figure 3.1: Illustration of the line-of-sight path and several macro-eigenrays travelling between the T_x and R_x in a shallow water acoustic channel.

The number of bounces between the bottom and surface can be large in shallow water acoustic (SWA) channels [6], with the energy being trapped in the waveguide. This differs from the fixed-to-mobile cellular radio channels, where single bounced eigenrays dominate [18], [19], and from mobile-to-mobile radio channels, where single- and double-bounced eigenrays dominate [20]. It is interesting to note that the number of different macro-eigenrays that arrive at the R_x, as determined experimentally in medium and long rage acoustic channels, is rarely larger than

eight [11], [21], [22]. Therefore, it cannot simply be assumed a large number of macro-eigenrays. Additionally, the waveguide geometry and the number of macro-eigenrays are the only indicators of which locations the eigenrays will interact with the surface and bottom of the waveguide, since the locations are deterministic [6]. Because of this, the macro-eigenrays can be modeled using the deterministic ray-tracing theory.

Each of the macro-eigenrays contain random signal fluctuations (micro-eigenrays), which represent the time variability of the channel impulse response [9], [6]. Random micro-scatterers can be used to characterize the roughness of the sea surface and sea bottom, as shown in Fig. 3.2. Each macro-eigenray can then be modeled as the average of a large number of micro-eigenrays, as shown in Fig. 3.2. The positions of the micro-scatterers are grouped around the location of the macro-scatterers to achieve this. These positions can be contrasted with radio channel propagation, where the scatterers can be placed randomly in a 2-D or 3-D plane.

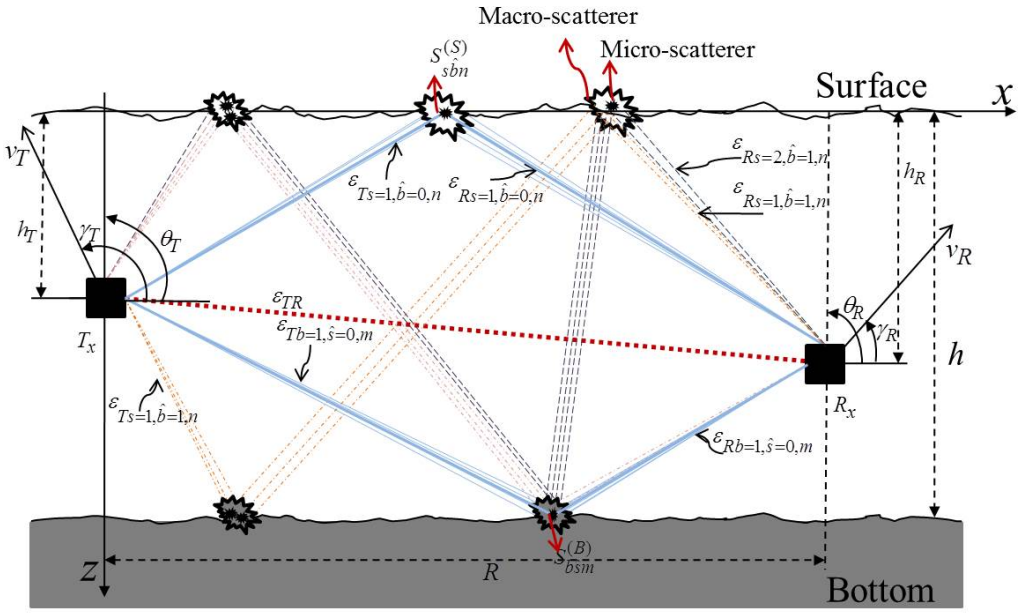

Figure 3.2: The geometry-based model for UV-to-UV SWA channels. Each macro-eigenray is represented as a large number of micro-eigenrays.

The underwater acoustic channel model of [17] is based on the following assumptions:

- (i) propagation occurs at a constant sound speed in a shallow water environment, i.e., sound energy propagates along plane waves;
- (ii) the $\mathrm{T_x}$ is an omnidirectional transducer, producing a spherical wavefront in this isovelocity medium;
- (iii) propagation is characterized with either line-of-sight (LoS) or non-line-of-sight (NLoS) conditions between the $\mathrm{T_x}$ and $\mathrm{R_x}$.

The depths of $\mathrm{T_x}$ and $\mathrm{R_x}$ are denoted by h_T and h_R, respectively, with the orientations of the $\mathrm{T_x}$ and $\mathrm{R_x}$ transducer arrays in the x-z plane denoted by θ_T and θ_R, respectively, relative to the x-axis. The $\mathrm{T_x}$ and $\mathrm{R_x}$ are moving with constant speeds v_T and v_R in the directions described by angles γ_T and γ_R in the x-z plane (relative to the x-axis), respectively.

The $\mathrm{R_x}$ receives $2S$ downward arriving (DA) macro-eigenrays, whose last reflection was from the surface, at any instant in time t. Each of these macro-eigenrays has a different number of s surface and $\hat{b}$ bottom reflections, S denoting the maximum number of interactions between any DA macro-eigenray and the surface, $1 \leq s \leq S$, and $s - 1 \leq \hat{b} \leq s$. For example, if a DA macro-eigenray interacts once with the surface, i.e., $S = 1$, then there are two paths that this eigenray could have traveled. The first is a single-bounced path, where a DA macro-eigenray started upwards, reflected from the surface, and arrived at the $\mathrm{R_x}$, i.e., $s = 1, \hat{b} = 0$. The second path is a double-bounced path, where a DA macro-eigenray started downwards, reflected from the bottom, then reflected from the surface, arriving at the $\mathrm{R_x}$, i.e., $s = 1, \hat{b} = 1$. Note that for $S = 1$, both macro-eigenrays will reach the $\mathrm{R_x}$ since they have similar energy [11], [6]. For the opposite case, there are $2B$ upward arriving (UA) macro-eigenrays, where the last reflection is from the bottom. These

macro-eigenrays have b bottom and $\hat{s}$ surface reflections, where B denotes the maximum number of interactions between a UA macro-eigenray and the bottom, $1 \leq b \leq B$ and $b-1 \leq \hat{s} \leq b$. As noted above, each DA macro-eigenray is modeled as an average of $N_{s\hat{b}}$ DA micro-eigenrays, and each UA macro-eigenray is modeled as an average of $M_{b\hat{s}}$ UA micro-eigenrays.

The symbols $\alpha_{Ts\hat{b}n}$ and $\alpha_{Tb\hat{s}m}$ represent the angles of departure (AoD) of micro-eigenrays originating from T_x and arriving at the scatterers $S^{(S)}_{s\hat{b}n}$ and $S^{(B)}_{b\hat{s}m}$, respectively. Likewise, $\alpha_{Rs\hat{b}n}$ and $\alpha_{Rb\hat{s}m}$ are the angles of arrival (AoA) of the micro-eigenrays scattered from $S^{(S)}_{s\hat{b}n}$ and $S^{(B)}_{b\hat{s}m}$ and arriving at R_x, respectively. Finally, the symbol α_{TR} denotes the AoA of the LoS ray. Fig. 3.3 details the geometry of the LoS path as well as the geometry of single-bounced surface and single-bounced bottom micro-eigenrays (i.e., $s=1, \hat{b}=0$, $b=1, \hat{s}=0$) scattered from the $S^{(S)}_{s=1,\hat{b}=0,n}$-th and $S^{(B)}_{b=1,\hat{s}=0,m}$-th micro-scatterers, respectively. The geometry of multiple-bounced micro-eigenrays is defined similarly, but omitted from Fig. 3.3 for ease of reference.

The horizontal distance between the $\mathrm{T_x}$ and $\mathrm{R_x}$ is called R and the water depth is h. Since medium- and long-range shallow-water communications is the subject of interest, it is assumed that the depths h, h_T, and h_R are much smaller than the distance R. The symbols $\epsilon_{Ts\hat{b}n}$ and $\epsilon_{Tb\hat{s}m}$ represent distances T_x-$S^{(S)}_{s\hat{b}n}$ and T_x-$S^{(B)}_{b\hat{s}m}$, respectively, where $S^{(S)}_{s\hat{b}n}$ and $S^{(B)}_{b\hat{s}m}$ represent the n^{th} and m^{th} micro-scatterers located around the macro-scatterers $S^{(S)}_{s\hat{b}}$ and $S^{(B)}_{b\hat{s}}$ at the surface and bottom, respectively, for $1 \leq n \leq N_{s\hat{b}}$ and $1 \leq m \leq M_{b\hat{s}}$. Finally, ϵ_{TR} denotes the distance T_x-R_x.

With frequency-flat fading, the complex faded envelope can be written as the superposition of the LoS, UA bounced macro-eigenrays, and DA bounced maro-eigenrays. Each UA and DA macro-eigenray is represented by an average of $M_{b\hat{s}}$ UA and $N_{s\hat{b}}$ DA micro-eigenrays, respectively. The channel impulse response

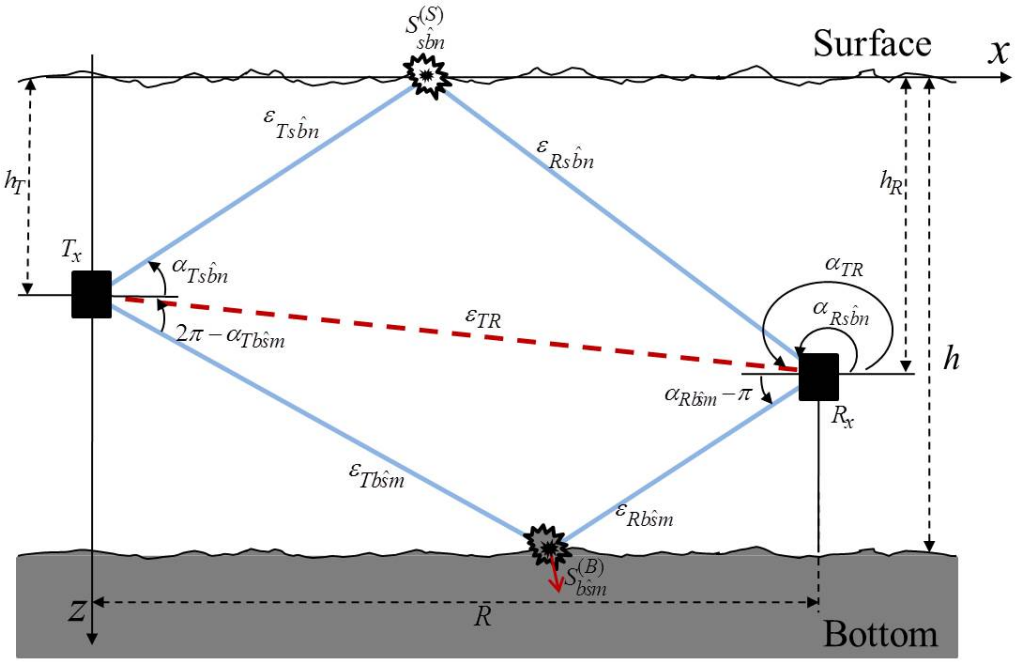

Figure 3.3: The detailed geometry of the LoS path, single-bounced surface and single-bounced bottom micro-eigenrays scattered from the $S^{(S)}_{s,\hat{b},n}$ and $S^{(B)}_{b,\hat{s},m}$ micro-scatterers, respectively.

between the T_x and R_x is then [17]

$$h(t) \;=\; h^{LoS}(t) + h^{UA}(t) + h^{DA}(t), \tag{3.1}$$

where the the respective components are [17]

$$h^{LoS}(t) \;=\; \sqrt{\Omega}\cdot a^{LoS}\cdot e^{j2\pi f^{LoS}t}, \tag{3.2}$$

$$h^{UA}(t) \;=\; \sqrt{\Omega}\sum_{b=1}^{B}\sum_{\hat{s}=b-1}^{b}\lim_{M_{b\hat{s}}\to\infty}\sum_{m=1}^{M_{b\hat{s}}} a^{UA}_{b\hat{s}m}\cdot e^{j(2\pi f^{UA}_{b\hat{s}m}t+\phi^{UA}_{b\hat{s}m})}, \tag{3.3}$$

$$h^{DA}(t) \;=\; \sqrt{\Omega}\sum_{s=1}^{S}\sum_{\hat{b}=s-1}^{s}\lim_{N_{s\hat{b}}\to\infty}\sum_{n=1}^{N_{s\hat{b}}} a^{DA}_{s\hat{b}n}\cdot e^{j(2\pi f^{DA}_{s\hat{b}n}t+\phi^{DA}_{s\hat{b}n})}, \tag{3.4}$$

and where Ω is the averaged total power ($\sqrt{\Omega}$ is assumed to be constant). The channel gains, Doppler shift frequencies, and phases in this model can be calculated as follows:

- **Channel gains**. The model's channel gains are normalized so that the

ensemble averages of the $a_{b\hat{s}m}^{UA}$'s and $a_{s\hat{b}n}^{DA}$'s are

$$\sum_{b=1}^{B}\sum_{\hat{s}=b-1}^{b}\sum_{m=1}^{M_{b\hat{s}}} E[{a_{b\hat{s}m}^{UA}}^2] = 1, \tag{3.5}$$

$$\sum_{s=1}^{S}\sum_{\hat{b}=s-1}^{s}\sum_{n=1}^{N_{s\hat{b}}} E[{a_{s\hat{b}n}^{DA}}^2] = 1. \tag{3.6}$$

The division of the total signal power between the LoS and NLoS components is described by the parameter K: the power allocated to the LoS component is $K/(1+K)$, while the total power allocated to the NLoS components is $1/(1+K)$. It is assumed that the relative power allocated to the UA and DA components is η_B and η_S respectively, and that $\eta_B + \eta_S = 1$. These parameters must be either set during simulations or estimated from measurements. With this, the channel gains can be written as follows:

$$a^{LoS} = \sqrt{\frac{K}{K+1}}, \tag{3.7}$$

$$a_{b\hat{s}m}^{UA} = \sqrt{\frac{1}{K+1}}\sqrt{\frac{\eta_B}{2B}}\sqrt{\frac{1}{M_{b\hat{s}}}}, \tag{3.8}$$

$$a_{s\hat{b}n}^{DA} = \sqrt{\frac{1}{K+1}}\sqrt{\frac{\eta_S}{2S}}\sqrt{\frac{1}{N_{s\hat{b}}}}. \tag{3.9}$$

- **Doppler Shifts**. Doppler shifts are dependent on the vertical displacements of surface micro-scatterers due to surface motion ($\Delta Z_{s\hat{b}n}(t)$ and $\Delta Z_{b\hat{s}m}(t)$), the geometrical relation between directions of movement of $\mathrm{T_x}$ and $\mathrm{R_x}$ (γ_T and γ_R), and the directions of AoDs and AoAs. For this model, the Doppler shifts are

$$f^{LoS} = f_{\mathrm{Tmax}}\cos(\alpha_{TR}+\pi-\gamma_T) + f_{\mathrm{Rmax}}\cos(\alpha_{TR}-\gamma_R), \tag{3.10}$$

$$\begin{aligned} f_{b\hat{s}m}^{UA} &= \frac{1}{\lambda t}\Delta Z_{b\hat{s}m}(t)\sin\alpha_{Rb\hat{s}m} + f_{\mathrm{Tmax}}\cos(\alpha_{Tb\hat{s}m}-\gamma_T) \\ &+ f_{\mathrm{Rmax}}\cos(\alpha_{Rb\hat{s}m}-\gamma_R), \end{aligned} \tag{3.11}$$

$$\begin{aligned} f_{s\hat{b}n}^{DA} &= \frac{1}{\lambda t}\Delta Z_{s\hat{b}n}(t)\sin\alpha_{Rs\hat{b}n} + f_{\mathrm{Tmax}}\cos(\alpha_{Ts\hat{b}n}-\gamma_T) \\ &+ f_{\mathrm{Rmax}}\cos(\alpha_{Rs\hat{b}n}-\gamma_R), \end{aligned} \tag{3.12}$$

with $f_{\text{Tmax}} = v_T/\lambda$ and $f_{\text{Rmax}} = v_R/\lambda$ being the maximum Doppler frequencies associated with the T_x and R_x, respectively, and λ being the carrier wavelength. Because the scatterers' locations are not known *a priori*, random variables are used to model the angles-of-departure $\alpha_{Ts\hat{b}n}$ and $\alpha_{Tb\hat{s}m}$, the angles-of-arrival $\alpha_{Rs\hat{b}n}$ and $\alpha_{Rb\hat{s}m}$, and the vertical displacements $\Delta Z_{s\hat{b}n}(t)$ and $\Delta Z_{b\hat{s}m}(t)$. These discrete random variables become continuous since the number of micro-eigenrays approaches infinity, with probability density functions (pdf)s $p(\alpha_{Ts\hat{b}})$, $p(\alpha_{Tb\hat{s}})$, $p(\alpha_{Rs\hat{b}})$, $p(\alpha_{Rb\hat{s}})$, $p(\Delta Z_{s\hat{b}}(t))$, and $p(\Delta Z_{b\hat{s}}(t))$, respectively. Because the relationship between the AoDs and the AoAs is determined by the geometry that propagating waves encounter while traveling from the transmitter to the receiver, the AoAs ($\alpha_{Rs\hat{b}n}$ and $\alpha_{Rb\hat{s}m}$) are dependent on the AoDs ($\alpha_{Ts\hat{b}n}$ and $\alpha_{Tb\hat{s}m}$, respectively). Assuming that each micro-eigenray has equal incident and reflecting angles when interacting with the surface and the bottom, then $\alpha_{Ts\hat{b}n} = \pi - \alpha_{Rs\hat{b}n}$ and $\alpha_{Tb\hat{s}m} = 3\pi - \alpha_{Rb\hat{s}m}$.

- **Phases**. A phase shift introduced by a scatterer near the T_x is independent of the phase shift introduced by a scatterer located near the R_x. Therefore, it can be assumed without loss of generality, that the phases $\phi_{s\hat{b}n}$ and $\phi_{b\hat{s}m}$ are independent random variables. Because the number of micro-eigenrays approaches infinity, these discrete random variables become continuous with pdfs $p(\phi_{s\hat{b}})$ and $p(\phi_{b\hat{s}})$, respectively. It is assumed that they are uniformly distributed on the interval $[-\pi, \pi)$ and independent from any other random variable.

3.4 Temporal Fading Characteristics of UV-to-UV Frequency Flat Acoustic Fading Channels

Using the resulting model from the previous section, the key temporal characteristics of the UV-to-UV frequency flat acoustic fading channels, such as

temporal autocorrelation funtion, Doppler spectrum, and level crossing rate, can now be derived.

3.4.1 Temporal Autocorrelation Function

The temporal autocorrelation function (ACF) allows quantification of necessary communication parameters such as the required number of pilot symbols and the system performance degradation, making it an important quantity. The normalized ACF is defined as

$$R(\tau) = \frac{\mathrm{E}\left[h(t)h(t+\tau)^*\right]}{\sqrt{\mathrm{Var}[h(t)]\mathrm{Var}[h(t+\tau)^*]}}, \tag{3.13}$$

where the variance Var[·] and the expected value E[·] are with respect to the random variables $\alpha_{Rs\hat{b}}$, $\alpha_{Rb\hat{s}}$, $\Delta Z_{s\hat{b}}(t)$, $\Delta Z_{b\hat{s}}(t)$, $\phi_{s\hat{b}}$, and $\phi_{b\hat{s}}$.

The angles of arrival $\alpha_{Rs\hat{b}}$ and $\alpha_{Rb\hat{s}}$ are modeled with the following Gaussian probability density functions [17]

$$p_{\mathrm{top}}(\alpha_{Rs\hat{b}}) = \frac{1}{\sqrt{2\pi\sigma^2_{DAs\hat{b}}}} \exp\{-(\alpha_{Rs\hat{b}} - \mu_{DAs\hat{b}})^2/(2\sigma^2_{DAs\hat{b}})\},\ 0 < \alpha_{Rs\hat{b}} < \pi, \tag{3.14}$$

$$p_{\mathrm{bottom}}(\alpha_{Rb\hat{s}}) = \frac{1}{\sqrt{2\pi\sigma^2_{UAb\hat{s}}}} \exp\{-(\alpha_{Rb\hat{s}} - \mu_{UAb\hat{s}})^2/(2\sigma^2_{UAb\hat{s}})\},\ \pi < \alpha_{Rb\hat{s}} < 2\pi, \tag{3.15}$$

with $\mu_{DAs\hat{b}}$ and $\mu_{UAb\hat{s}}$ being the mean AoAs, and $\sigma_{DAs\hat{b}}$ and $\sigma_{UAb\hat{s}}$ being the angle spreads. The vertical displacements $\Delta Z_{s\hat{b}}(t)$ and $\Delta Z_{b\hat{s}}(t)$ are modeled as zero-mean Gaussian random processes with stationary and independent increments and can be written as

$$p(\Delta Z_{s\hat{b}}(t)) = \frac{1}{\sqrt{2\pi t\zeta^2_{\Delta Z_{DAs\hat{b}}}}} \exp(-(\Delta Z_{s\hat{b}}(t))^2/(2t\zeta^2_{\Delta Z_{DAs\hat{b}}})) \tag{3.16}$$

$$p(\Delta Z_{b\hat{s}}(t)) = \frac{1}{\sqrt{2\pi t\zeta^2_{\Delta Z_{UAb\hat{s}}}}} \exp(-(\Delta Z_{b\hat{s}}(t))^2/(2t\zeta^2_{\Delta Z_{UAb\hat{s}}})), \tag{3.17}$$

where $t\zeta^2_{\Delta Z_{DAs\hat{b}}}$ and $t\zeta^2_{\Delta Z_{UAb\hat{s}}}$ denote their respective variances.

Different macro-eigenrays have different angles of departure and arrival. Because of this, the locations of the micro-eigenrays that make up one macro-eigenray are

independent from the locations of those that make up another macro-eigenray. Using the Central Limit Theorem [19] along with the assumptions above, each macro-eigenray can be considered as am independent complex zero-mean Gaussian process. Since the sum of complex zero-mean Gaussian processes leads to a new complex zero-mean Gaussian process, $h^{UA}(t)$ and $h^{DA}(t)$ are then also independent comples zero-mean Gaussian processes. The normalized ACF can then be simplified to

$$R(\tau) \;=\; R^{LoS}(\tau) + R^{UA}(\tau) + R^{DA}(\tau), \tag{3.18}$$

where $R^{LoS}(\tau)$, $R^{UA}(\tau)$, and $R^{DA}(\tau)$ are the normalized ACFs of the LoS, upward-arriving, and downward-arriving eigenrays, respectively.

The temporal ACF of the LoS component of the signal can be found as follows

$$\begin{aligned} R^{LoS}(\tau) &= \frac{\mathrm{E}\left[h^{LoS}(t)h^{LoS}(t+\tau)^*\right]}{\sqrt{\mathrm{Var}[h^{LoS}(t)]\mathrm{Var}[h^{LoS}(t+\tau)^*]}} \\ &= \frac{K}{K+1}e^{j2\pi\tau[f_{\mathrm{Tmax}}\cos(\alpha_{TR}-\gamma_T)-f_{\mathrm{Rmax}}\cos(\alpha_{TR}-\gamma_R)]}. \end{aligned} \tag{3.19}$$

Since the phases $\phi_{b\hat{s}m}$ and $\phi_{s\hat{b}n}$ are independent and uniformly distributed over $[-\pi,\pi)$, the ACFs of the UA and DA components can be written as

$$\begin{aligned} R^{UA}(\tau) &= \frac{\mathrm{E}\left[h^{UA}(t)h^{UA}(t+\tau)^*\right]}{\sqrt{\mathrm{Var}[h^{UA}(t)]\mathrm{Var}[h^{UA}(t+\tau)^*]}} \\ &= \frac{\eta_B}{2B(K+1)}\sum_{b=1}^{B}\sum_{\hat{s}=b-1}^{b}\sum_{m=1}^{M_{b\hat{s}}}\mathrm{E}[a_{b\hat{s}m}^2] \\ &\quad \exp\left(j2\pi\tau\left[f_{\mathrm{Tmax}}\cos(\alpha_{Rb\hat{s}m}+\gamma_T)-f_{\mathrm{Rmax}}\cos(\alpha_{Rb\hat{s}m}-\gamma_R)\right]\right) \\ &\quad \mathrm{E}_{\Delta Z_{b\hat{s}m}(t)}\left[\exp\left(-j\frac{2\pi}{\lambda}(\Delta Z_{b\hat{s}m}(t+\tau)-\Delta Z_{b\hat{s}m}(t))\sin\alpha_{Rb\hat{s}m}\right)\right], \end{aligned} \tag{3.20}$$

$$\begin{aligned} R^{DA}(\tau) &= \frac{\mathrm{E}\left[h^{DA}(t)h^{DA}(t+\tau)^*\right]}{\sqrt{\mathrm{Var}[h^{DA}(t)]\mathrm{Var}[h^{DA}(t+\tau)^*]}} \\ &= \frac{\eta_S}{2S(K+1)}\sum_{s=1}^{S}\sum_{\hat{b}=s-1}^{s}\sum_{n=1}^{N_{s\hat{b}}}\mathrm{E}[a_{s\hat{b}n}^2] \\ &\quad \exp\left(j2\pi\tau\left[f_{\mathrm{Tmax}}\cos(\alpha_{Rs\hat{b}n}+\gamma_T)-f_{\mathrm{Rmax}}\cos(\alpha_{Rs\hat{b}n}-\gamma_R)\right]\right) \\ &\quad \mathrm{E}_{\Delta Z_{s\hat{b}n}(t)}\left[\exp\left(-j\frac{2\pi}{\lambda}(\Delta Z_{s\hat{b}n}(t+\tau)-\Delta Z_{s\hat{b}n}(t))\sin\alpha_{Rs\hat{b}n}\right)\right], \end{aligned} \tag{3.21}$$

where $\mathrm{E}_{\Delta Z_{b\hat{s}m}(t)}[\cdot]$ and $\mathrm{E}_{\Delta Z_{s\hat{b}n}(t)}[\cdot]$ denote the statistical expectations with respect to $\Delta Z_{b\hat{s}m}(t)$ and $\Delta Z_{s\hat{b}n}(t)$, respectively.

With a large number of macro-eigenrays, such as $M_{b\hat{s}} \gg 1$ and $N_{s\hat{b}} \gg 1$, continuous random variables $\alpha_{Rb\hat{s}}$ and $\alpha_{Rs\hat{b}}$ characterized with pdfs $p_{\text{bottom}}(\alpha_{Rb\hat{s}})$ and $p_{\text{top}}(\alpha_{Rs\hat{b}})$ respectively, can replace the discrete angles-of-arrival $\alpha_{Rb\hat{s}m}$ and $\alpha_{Rs\hat{b}n}$. The summations $\sum_{m=1}^{M_{b\hat{s}}}$ and $\sum_{n=1}^{N_{s\hat{b}}}$ in (3.20) and (3.21) can be replaced by integrals

$$\begin{aligned} R^{UA}(\tau) &= \frac{\eta_B}{2B(K+1)} \sum_{b=1}^{B} \sum_{\hat{s}=b-1}^{b} \\ &\int_{\pi}^{2\pi} \exp\left(j2\pi\tau\left[f_{\text{Tmax}}\cos(\alpha_{Rb\hat{s}m}+\gamma_T) - f_{\text{Rmax}}\cos(\alpha_{Rb\hat{s}m}-\gamma_R)\right]\right) \\ &\mathrm{E}_{\Delta Z_{b\hat{s}m}(t)}\left[\exp\left(-j\frac{2\pi}{\lambda}(\Delta Z_{b\hat{s}m}(t+\tau) - \Delta Z_{b\hat{s}m}(t))\sin\alpha_{Rb\hat{s}m}\right)\right] d\alpha_{Rb\hat{s}}, \end{aligned} \tag{3.22}$$

$$\begin{aligned} R^{DA}(\tau) &= \frac{\eta_S}{2S(K+1)} \sum_{s=1}^{S} \sum_{\hat{b}=s-1}^{s} \\ &\int_{0}^{\pi} \exp\left(j2\pi\tau\left[f_{\text{Tmax}}\cos(\alpha_{Rs\hat{b}n}+\gamma_T) - f_{\text{Rmax}}\cos(\alpha_{Rs\hat{b}n}-\gamma_R)\right]\right) \\ &\mathrm{E}_{\Delta Z_{s\hat{b}n}(t)}\left[\exp\left(-j\frac{2\pi}{\lambda}(\Delta Z_{s\hat{b}n}(t+\tau) - \Delta Z_{s\hat{b}n}(t))\sin\alpha_{Rs\hat{b}n}\right)\right] d\alpha_{Rs\hat{b}}. \end{aligned} \tag{3.23}$$

Because $\Delta Z_{b\hat{s}}(t)$ has stationary and independent increments with pdfs defined in (3.17), the expected value $\mathrm{E}_{\Delta Z_{b\hat{s}}(t)}[\cdot]$ in (3.22) can be determined as follows

$$\begin{aligned} &\mathrm{E}_{\Delta Z_{b\hat{s}m}(t)}\left[\exp\left(-j\frac{2\pi}{\lambda}(\Delta Z_{b\hat{s}m}(t+\tau) - \Delta Z_{b\hat{s}m}(t))\sin\alpha_{Rb\hat{s}m}\right)\right] = \\ &= \int_{-\infty}^{\infty} \exp\left(-j\frac{2\pi}{\lambda}(\Delta Z_{b\hat{s}}(t+\tau) - \Delta Z_{b\hat{s}}(t))\sin\alpha_{Rb\hat{s}}\right) \\ &\quad p(\Delta Z_{b\hat{s}}(t+\tau) - \Delta Z_{b\hat{s}}(t)) d(\Delta Z_{b\hat{s}}(t+\tau) - \Delta Z_{b\hat{s}}(t)) \\ &= \exp\left\{-\frac{\tau\zeta^2_{\Delta Z_{UAb\hat{s}}}}{2}\left[\frac{2\pi}{\lambda}\sin\alpha_{Rb\hat{s}}\right]^2\right\}. \end{aligned} \tag{3.24}$$

Similarly, the expectated value $\mathrm{E}_{\Delta Z_{s\hat{b}}(t)}[\cdot]$ in (3.23) becomes

$$\mathrm{E}_{\Delta Z_{s\hat{b}n}(t)}\left[\exp\left(-j\frac{2\pi}{\lambda}(\Delta Z_{s\hat{b}n}(t+\tau)-\Delta Z_{s\hat{b}n}(t))\sin\alpha_{Rs\hat{b}n}\right)\right] =$$
$$= \exp\left\{-\frac{\tau\zeta^2_{\Delta Z_{DAs\hat{b}}}}{2}\left[\frac{2\pi}{\lambda}\sin\alpha_{Rs\hat{b}}\right]^2\right\}. \tag{3.25}$$

Substituting (3.24) and (3.15) into (3.22), and (3.25) and (3.14) into (3.23), the ACFs of the UA and DA components, respectively, are:

$$\begin{aligned} R^{UA}(\tau) &= \frac{\eta_B}{2B(K+1)}\sum_{b=1}^{B}\sum_{\hat{s}=b-1}^{b}\int_{\pi}^{2\pi}\frac{1}{\sqrt{2\pi\sigma^2_{UAb\hat{s}}}}\exp\left(-\frac{(\alpha_{Rb\hat{s}}-\mu_{UAb\hat{s}})^2}{(2\sigma^2_{UAb\hat{s}})}\right) \\ &\quad \exp\left(j2\pi\tau\left[f_{\mathrm{Tmax}}\cos(\alpha_{Rb\hat{s}}+\gamma_T)-f_{\mathrm{Rmax}}\cos(\alpha_{Rb\hat{s}}-\gamma_R)\right]\right) \\ &\quad \exp\left(-\frac{\tau\zeta^2_{\Delta Z_{UAb\hat{s}}}}{2}\left[\frac{2\pi}{\lambda}\sin\alpha_{Rb\hat{s}}\right]^2\right)d\alpha_{Rb\hat{s}}, \end{aligned} \tag{3.26}$$

$$\begin{aligned} R^{DA}(\tau) &= \frac{\eta_S}{2S(K+1)}\sum_{s=1}^{S}\sum_{\hat{b}=s-1}^{s}\int_{0}^{\pi}\frac{1}{\sqrt{2\pi\sigma^2_{DAs\hat{b}}}}\exp\left(-\frac{(\alpha_{Rs\hat{b}}-\mu_{DAs\hat{b}})^2}{(2\sigma^2_{DAs\hat{b}})}\right) \\ &\quad \exp\left(j2\pi\tau\left[f_{\mathrm{Tmax}}\cos(\alpha_{Rs\hat{b}}+\gamma_T)-f_{\mathrm{Rmax}}\cos(\alpha_{Rs\hat{b}}-\gamma_R)\right]\right) \\ &\quad \exp\left(-\frac{\tau\zeta^2_{\Delta Z_{DAs\hat{b}}}}{2}\left[\frac{2\pi}{\lambda}\sin\alpha_{Rs\hat{b}}\right]^2\right)d\alpha_{Rs\hat{b}}. \end{aligned} \tag{3.27}$$

For small angle spreads, the AoAs $\alpha_{Rs\hat{b}}$ and $\alpha_{Rb\hat{s}}$ are mainly concentrated around the mean AoAs $\mu_{DAs\hat{b}}$ and $\mu_{UAb\hat{s}}$, respectively. Using the first-order Taylor expansion, the AoA angles can be approximated as follows

$$\cos(\alpha_{Rs\hat{b}}) \approx \cos(\mu_{DAs\hat{b}}) - \sin(\mu_{DAs\hat{b}})(\alpha_{Rs\hat{b}}-\mu_{DAs\hat{b}}) \tag{3.28}$$

$$\sin(\alpha_{Rs\hat{b}}) \approx \sin(\mu_{DAs\hat{b}}) + \cos(\mu_{DAs\hat{b}})(\alpha_{Rs\hat{b}}-\mu_{DAs\hat{b}}) \tag{3.29}$$

$$\sin(\alpha_{Rs\hat{b}})^2 \approx \sin(\mu_{DAs\hat{b}})^2 + 2\sin(\mu_{DAs\hat{b}})\cos(\mu_{DAs\hat{b}})(\alpha_{Rs\hat{b}}-\mu_{DAs\hat{b}}) \tag{3.30}$$

$$\sin(\alpha_{Rs\hat{b}})^{-1} \approx \sin(\mu_{DAs\hat{b}})^{-1} - \cos(\mu_{DAs\hat{b}})(\alpha_{Rs\hat{b}}-\mu_{DAs\hat{b}})/\sin(\mu_{DAs\hat{b}})^{-2}, \tag{3.31}$$

and similar approximations can be made to the AoAs $\alpha_{Rb\hat{s}}$. Using these trigonometric approximations and the equality $\int e^{j\alpha x}(2\pi\sigma^2)^{-1/2}e^{-x^2/(2\sigma^2)}dx = e^{-\sigma^2\alpha^2/2}$ [13], the ACFs of the UA and DA

components can be written as

$$
\begin{aligned}
R^{UA}(\tau) &= \frac{\eta_B}{2B(K+1)} \sum_{b=1}^{B} \sum_{\hat{s}=b-1}^{b} \exp\left(-\frac{\tau \zeta^2_{\Delta Z_{UAb\hat{s}}}}{2} \left[\frac{2\pi}{\lambda} \sin \mu_{UAb\hat{s}} \right]^2 \right) \\
&\quad \exp(-j2\pi\tau \left[f_{\mathrm{Rmax}} \cos(\mu_{UAb\hat{s}} - \gamma_R) - f_{\mathrm{Tmax}} \cos(\mu_{UAb\hat{s}} + \gamma_T) \right]) \\
&\quad \exp\left\{ -\frac{\sigma^2_{UAb\hat{s}}}{2} \Bigg[2\pi\tau \left[f_{\mathrm{Rmax}} \sin(\mu_{UAb\hat{s}} - \gamma_R) - f_{\mathrm{Tmax}} \sin(\mu_{UAb\hat{s}} + \gamma_T) \right] \right. \\
&\quad \left. + \tau \zeta^2_{\Delta Z_{UAb\hat{s}}} \left[\frac{2\pi}{\lambda} \right]^2 \sin \mu_{UAb\hat{s}} \cos \mu_{UAb\hat{s}} \Bigg]^2 \right\}, \qquad (3.32) \\
R^{DA}(\tau) &= \frac{\eta_S}{2S(K+1)} \sum_{s=1}^{S} \sum_{\hat{b}=s-1}^{s} \exp\left(-\frac{\tau \zeta^2_{\Delta Z_{DAs\hat{b}}}}{2} \left[\frac{2\pi}{\lambda} \sin \mu_{DAs\hat{b}} \right]^2 \right) \\
&\quad \exp\left(j2\pi\tau \left[f_{\mathrm{Tmax}} \cos(\mu_{DAs\hat{b}} + \gamma_T) - f_{\mathrm{Rmax}} \cos(\mu_{DAs\hat{b}} - \gamma_R) \right] \right) \\
&\quad \exp\left\{ -\frac{\sigma^2_{DAs\hat{b}}}{2} \Bigg[2\pi\tau \left[f_{\mathrm{Rmax}} \sin(\mu_{DAs\hat{b}} - \gamma_R) - f_{\mathrm{Tmax}} \sin(\mu_{DAs\hat{b}} + \gamma_T) \right] \right. \\
&\quad \left. + \tau \zeta^2_{\Delta Z_{DAs\hat{b}}} \left[\frac{2\pi}{\lambda} \right]^2 \sin \mu_{DAs\hat{b}} \cos \mu_{DAs\hat{b}} \Bigg]^2 \right\}. \qquad (3.33)
\end{aligned}
$$

From (3.19), (3.32), and (3.33), it appears that the ACF of a shallow-water acoustic channel can be described by an *exponential function*. This agrees with experimentally obtained ACFs [3], [22], [21]. This result is different from the traditional Bessel-shaped ACFs usually seen in radio channels. This is because of the different propagation mechanisms in SWA and radio channels. To illustrate this exponential behavior, Fig. 3.4 plots the ACF $R(\tau)$ as a function of time.
This curve is obtained assuming that the carrier frequency is $f_c = 1.7$ kHz and the speed of sound is $c = 1500$ m/s. The distance between the $\mathrm{T_x}$ and $\mathrm{R_x}$ is set to $R = 2$ km, while the water, $\mathrm{T_x}$, and $\mathrm{R_x}$ depths are $h = 100$ m, $h_T = 50$ m, and $h_R = 50$ m, respectively. It is assumed that the $\mathrm{T_x}$ and $\mathrm{R_x}$ are stationary, i.e., $v_T = v_R = 0$ m/s. For illustration purposes, the rest of the model parameters are chosen to be: $K = 0.6$, $S = B = 1$, $\zeta_{\Delta Z_{DA10}} = \zeta_{\Delta Z_{DA11}} = \zeta_{\Delta Z_{UA10}} = \zeta_{\Delta Z_{UA11}} = 0.1$, $\eta_S = 0.6$, $\mu_{DA10} = 166^\circ$, $\mu_{DA11} = 163.5^\circ$, $\mu_{UA10} = 191.9^\circ$, $\mu_{UA11} = 192.9^\circ$, $\sigma_{DA10} = 2.5^\circ$, $\sigma_{DA11} = 4^\circ$, $\sigma_{UA10} = 2.4^\circ$, $\sigma_{UA11} = 3^\circ$, $\alpha_{TR} = 180^\circ$.

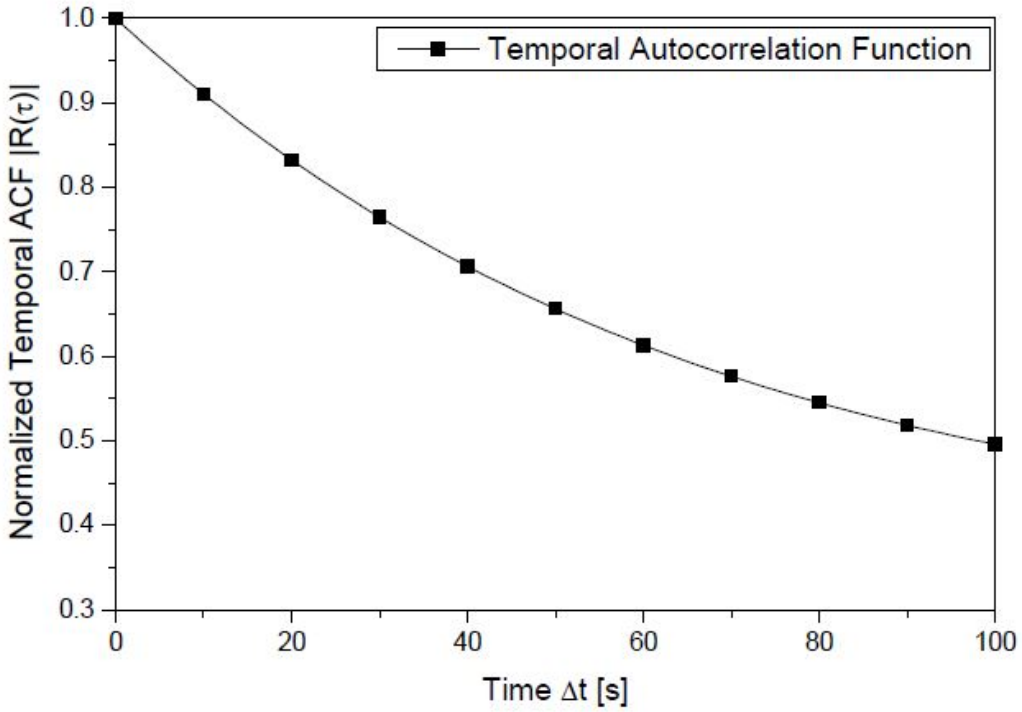

Figure 3.4: The magnitude of temporal autocorrelation function as a function of time.

3.5 Summary

This chapter described how the ocean environment is modeled as a waveguide, using ray tracing theory for sound propagation. The lack of consensus regarding statistical characterization of the underwater communication channel is noted. A proposed time varying shallow water acoustic channel is described in detail, with accompanying geometry. The channel impulse response is derived and explained. The autocorrelation function of the channel is also derived, taking into account several random variables accounting for random angles and ocean environmental factors. The autocorrelation function suggests that the channel can be described by an exponential function, different than autocorrelation functions of radio channels.

CHAPTER IV

LEVEL CROSSING RATE

4.1 Overview

The statistical properties of chapter 3 are drawn from for the derivations in the remainder of the thesis. This chapter contributes the new derivation of the level crossing rate of the underwater fading channel. The envelope level crossing rate (LCR) is a necessary statistic to be able to characterize system characteristics such as handoff, transmitter and receiver velocities, and fading rate. In order to derive the LCR, the time-varying model for the channel is used, which accounts for both the micro- and the macro-scattering effects [27], [17]. This model characterizes the sound propagation in shallow water isovelocity environments by applying the statistical methods necessary to characterize the random components of the propagation medium to the deterministic ray-tracing theory. The LCR is derived for the non-isotropic scattering environment, from the analytical model.

4.2 Level Crossing Rate in Mobile-to-Mobile Underwater Fading Channels

Assuming a 2-D non-isotropic scattering environment, the LCR of the complex faded envelope described in (3.1) is now derived. The LCR at a specified level R, $L(R)$, is defined as the rate at which the signal envelope crosses level R in the positive going direction. The LCR can be written as [19]

$$L(R) = \int_0^\infty \dot{\alpha} p_{\alpha,\dot{\alpha}}(R, \dot{\alpha}) d\dot{\alpha}, \tag{4.1}$$

where $\alpha = |h(t)|$ is the envelope level, $\dot{\alpha} = |\dot{h}(t)|$ is the envelope slope, and $p_{\alpha,\dot{\alpha}}(R, \dot{\alpha})$ is the joint probability density function (pdf) of the envelope level and

the envelope slope. First, it is observed that the envelope $|h(t)|$ of the model described earlier has a Ricean distribution. Then, the envelope slope $|\dot{h}(t)|$ has a Gaussian distribution. Furthermore, the joint pdf $p_{\alpha,\dot{\alpha}}(\alpha,\dot{\alpha})$ cannot be represented as a product of a Rice pdf $p_{|h(t)|}(\alpha)$ and a Gaussian pdf $p_{|\dot{h}(t)|}(\dot{\alpha})$, because the real and imaginary components of the complex faded envelope $h(t)$ are correlated. Hence, the LCR for LoS conditions (Ricean fading, correlated in-phase and quadrature components) can be written as [24]

$$\begin{aligned} L(R) &= \frac{R\sqrt{2\chi}}{\pi^{3/2}b_0}\, e^{-(R^2+\delta^2)/(2b_0)} \int_0^{\pi/2} \cosh\left(\frac{R\delta}{b_0}\cos\theta\right) \\ &\times \left[e^{-(\xi\delta\sin\theta)^2} + \sqrt{\pi}\xi\delta\sin\theta\ \mathrm{erf}(\xi\delta\sin\theta)\right] d\theta, \end{aligned} \tag{4.2}$$

where $\cosh(\cdot)$ is the hyperbolic cosine function and $\mathrm{erf}(\cdot)$ is the error function. The rest of the parameters are $\delta = \sqrt{K/(K+1)}$, $\chi = b_2 - b_1^2/b_0$,
$\xi = (2\pi f^{LoS} - b_1/b_0)/\sqrt{2\chi}$, and

$$b_0 \triangleq \mathrm{E}[h_i(t)^2] = \mathrm{E}[h_q(t)^2], \tag{4.3}$$

$$b_1 \triangleq \mathrm{E}[h_i(t)\dot{h}_q(t)] = \mathrm{E}[h_q(t)\dot{h}_i(t)], \tag{4.4}$$

$$b_2 \triangleq \mathrm{E}[\dot{h}_i(t)^2] = \mathrm{E}[\dot{h}_q(t)^2], \tag{4.5}$$

where $h_i(t)$ and $h_q(t)$ denote the real and imaginary part of $h(t)$, respectively, and $\dot{h}_i(t)$ and $\dot{h}_q(t)$ are first derivatives of $h_i(t)$ and $h_q(t)$ with respect to time t. When shallow water acoustic scattering is characterized using the probability density functions in (3.14)-(3.17), the closed-form expressions for b_0, b_1, and b_2 can be obtained by substituting (3.1) into (4.2). Parameter b_0 then becomes

$$2b_0 = 2b_0^{UA} + 2b_0^{DA} = \frac{1}{K+1}, \tag{4.6}$$

where b_0^{UA} and b_0^{DA} are, respectively,

$$\begin{aligned} 2b_0^{UA} &= \Re\{R^{UA}(\tau)_{\tau=0}\} \\ &= \frac{\eta_B}{(K+1)}, \end{aligned} \tag{4.7}$$

$$\begin{aligned} 2b_0^{DA} &= \Re\{R^{DA}(\tau)_{\tau=0}\} \\ &= \frac{\eta_S}{(K+1)}, \end{aligned} \tag{4.8}$$

and where $\Re\{\cdot\}$ denotes the real part operation. Similarly, parameters b_1 and b_2 can be obtained as follows:

$$b_n = b_n^{UA} + b_n^{DA}, \tag{4.9}$$

where $n \in \{1, 2\}$ and b_n^{UA} and b_n^{DA} can be written as

$$\begin{aligned} b_1^{UA} &= \Im\left\{\frac{1}{2}\frac{dR^{UA}(\tau)}{d\tau}_{\tau=0}\right\} \\ &= \frac{b_0}{2B}\sum_{b=1}^{B}\sum_{\hat{s}=b-1}^{b} 2\pi\Big[f_{\mathrm{Tmax}}\cos(\mu_{UAb\hat{s}} + \gamma_T) \\ &- f_{\mathrm{Rmax}}\cos(\mu_{UAb\hat{s}} - \gamma_R)\Big] \end{aligned} \tag{4.10}$$

$$\begin{aligned} b_1^{DA} &= \Im\left\{\frac{1}{2}\frac{dR^{DA}(\tau)}{d\tau}_{\tau=0}\right\} \\ &= \frac{b_0}{2S}\sum_{s=1}^{S}\sum_{\hat{b}=s-1}^{s} 2\pi\Big[f_{\mathrm{Tmax}}\cos(\mu_{DAs\hat{b}} + \gamma_T) \\ &- f_{\mathrm{Rmax}}\cos(\mu_{DAs\hat{b}} - \gamma_R)\Big] \end{aligned} \tag{4.11}$$

$$\begin{aligned} b_2^{UA} &= -\Re\left\{\frac{1}{2}\frac{d^2R^{UA}(\tau)}{d\tau^2}_{\tau=0}\right\} \\ &= \frac{b_0}{2B}\sum_{b=1}^{B}\sum_{\hat{s}=b-1}^{b} b_{UAb\hat{s}}^2 - a_{UAb\hat{s}}^2 + 2c_{UAb\hat{s}}, \end{aligned} \tag{4.12}$$

$$\begin{aligned} b_2^{DA} &= -\Re\left\{\frac{1}{2}\frac{d^2R^{DA}(\tau)}{d\tau^2}_{\tau=0}\right\} \\ &= \frac{b_0}{2S}\sum_{s=1}^{S}\sum_{\hat{b}=s-1}^{s} b_{DAs\hat{b}}^2 - a_{DAs\hat{b}}^2 + 2c_{DAs\hat{b}}, \end{aligned} \tag{4.13}$$

and where $\Im\{\cdot\}$ denotes the imaginary part operation, and $a_{UAb\hat{s}}$, $b_{UAb\hat{s}}$, $c_{UAb\hat{s}}$, $a_{DAs\hat{b}}$, $b_{DAs\hat{b}}$, and $c_{DAs\hat{b}}$ are, respectively,

$$
\begin{aligned}
a_{UAb\hat{s}} &= \frac{\zeta^2_{\Delta Z_{UAb\hat{s}}}}{2}\left[\frac{2\pi}{\lambda}\sin\mu_{UAb\hat{s}}\right]^2, && (4.14)\\
b_{UAb\hat{s}} &= 2\pi\Bigg[f_{\mathrm{Rmax}}\cos(\mu_{UAb\hat{s}}-\gamma_R)\\
&- f_{\mathrm{Tmax}}\cos(\mu_{UAb\hat{s}}+\gamma_T)\Bigg], && (4.15)\\
c_{UAb\hat{s}} &= \frac{\sigma^2_{UAb\hat{s}}}{2}\Bigg[2\pi\Bigg[f_{\mathrm{Rmax}}\sin(\mu_{UAb\hat{s}}-\gamma_R)\\
&- f_{\mathrm{Tmax}}\sin(\mu_{UAb\hat{s}}+\gamma_T)\Bigg]\\
&+ \zeta^2_{\Delta Z_{UAb\hat{s}}}\left[\frac{2\pi}{\lambda}\right]^2\sin\mu_{UAb\hat{s}}\cos\mu_{UAb\hat{s}}\Bigg]^2, && (4.16)\\
a_{DAs\hat{b}} &= \frac{\zeta^2_{\Delta Z_{DAs\hat{b}}}}{2}\left[\frac{2\pi}{\lambda}\sin\mu_{DAs\hat{b}}\right]^2, && (4.17)\\
b_{DAs\hat{b}} &= 2\pi\Bigg[f_{\mathrm{Rmax}}\cos(\mu_{DAs\hat{b}}-\gamma_R)\\
&- f_{\mathrm{Tmax}}\cos(\mu_{DAs\hat{b}}+\gamma_T)\Bigg], && (4.18)\\
c_{DAs\hat{b}} &= \frac{\sigma^2_{DAs\hat{b}}}{2}\Bigg[2\pi\Bigg[f_{\mathrm{Rmax}}\sin(\mu_{DAs\hat{b}}-\gamma_R)\\
&- f_{\mathrm{Tmax}}\sin(\mu_{DAs\hat{b}}+\gamma_T)\Bigg]\\
&+ \zeta^2_{\Delta Z_{DAs\hat{b}}}\left[\frac{2\pi}{\lambda}\right]^2\sin\mu_{DAs\hat{b}}\cos\mu_{DAs\hat{b}}\Bigg]^2. && (4.19)
\end{aligned}
$$

In the presence of shadowing, the envelope $|h(t)|$ can be modeled using the extended Suzuki process, i.e., as a product of the Ricean process with cross-correlated components and the log-normal process. The LCR for LoS conditions with shadowing can thus be written as [24]

$$
\begin{aligned}
L(R) = \frac{R\sqrt{2\chi}}{\pi^{3/2}b_0}\int_0^\infty \frac{F(R,l)}{l}\frac{e^{-\frac{(\ln l)^2}{2\sigma^2}}}{\sqrt{2\pi}\sigma l}\; e^{-((R/l)^2+\delta^2)/(2b_0)}\\
\int_0^{\pi/2}\cosh\left(\frac{R\delta}{lb_0}\cos\theta\right)\Bigg[e^{-\left(\frac{\xi\delta\sin\theta}{F(R,l)}\right)^2}\\
+\sqrt{\pi}\xi\delta\frac{\sin\theta}{F(R,l)}\;\mathrm{erf}\left(\xi\delta\frac{\sin\theta}{F(R,l)}\right)\Bigg]d\theta dl, \qquad (4.20)
\end{aligned}
$$

where $\cosh(\cdot)$ is the hyperbolic cosine function, $\text{erf}(\cdot)$ is the error function, and σ is the variance of shadow process. The rest of the parameters are $\delta = \sqrt{K/(K+1)}$, $\chi = b_2 - b_1^2/b_0$, $\xi = (2\pi f^{LoS} - b_1/b_0)/\sqrt{2\chi}$, $F(R,l) = \sqrt{1+(\gamma/\chi)(\sigma R/l)^2}$, $\gamma = 2/L_c^2$, and L_c is the correlation distance.

4.3 Comparison Between Analytical and Measured Level Crossing Rate

To verify the analytical LCR, the theoretical results are compared with those obtained from measured data. The experimental data was collected during the NRL ACOMMS09 experiment, held near the New Jersey shore in May 2009. The channel measurements are collected at $f_c = 17$ kHz and the speed of sound is $c = 1440$ m/s. The distance between the T_x and R_x was $R = 1.5$ km. The water, T_x, and R_x depths were $h = 80$ m, $h_T = 41$ m, and $h_R = 45$ m, respectively. It is assumed that the T_x and R_x are relatively stationary, i.e., slightly moving with waves (i.e., $\gamma_T = \gamma_R = 90°$).

Figs. 4.1 and 4.2 compare the analytical LCRs with and without shadowing with the measured LCRs with and without shadowing, respectively. The analytical curves in Figs. 4.1 and 4.2 are obtained with the parameters $K = 0.56$, $S = B = 1$, $v_T = v_R = 0.001$ m/s, $\mu_{DA10} = 168.5°$, $\mu_{DA11} = 167.5°$, $\mu_{UA10} = 185.5°$, $\mu_{UA11} = 186°$, $\sigma_{DA10} = 1.4°$, $\sigma_{DA11} = 1.9°$, $\sigma_{UA10} = 2.1°$, $\sigma_{UA11} = 2.6°$, $\zeta_{\Delta Z_{DA10}} = \zeta_{\Delta Z_{DA11}} = 0.9$, $\zeta_{\Delta Z_{UA10}} = \zeta_{\Delta Z_{UA11}} = 1.6$, $\gamma = 0.621$, $\sigma = 3.55$, $\eta_S = 0.58$, and $\eta_B = 1 - \eta_S$. The Rice factor K is estimated using the moment-method in [25]. The rest of the parameters, i.e., $[v_T, v_R, \zeta_{\Delta Z_{DAsb}}, \zeta_{\Delta Z_{UAbs}}, \mu_{DAsb}, \mu_{UAbs}, \sigma_{DAsb}, \sigma_{UAbs}, \eta_S]$ are estimated jointly using the maximum-likelihood approach in [20] and the constraint $\eta_S + \eta_B = 1$. The close agreement between the analytical and measured LCRs in Figs. 4.1 and 4.2 confirms the utility of the derived statistics.

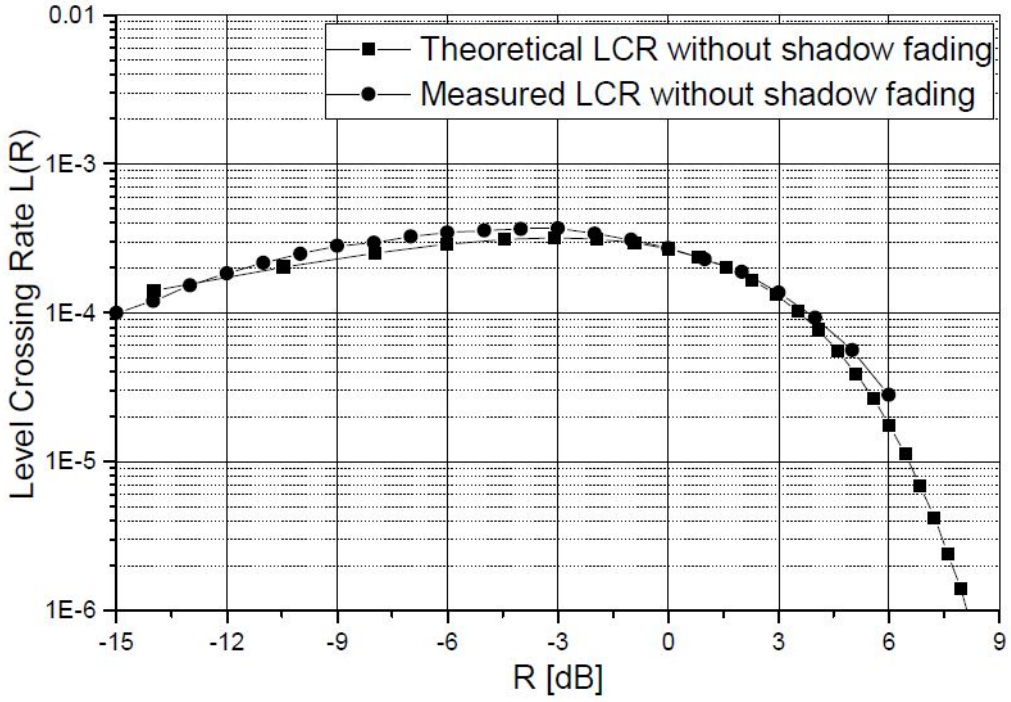

Figure 4.1: Theoretical and measured level crossing rates *without* shadow fading.

4.4 Summary

This chapter presents and describes a method for calculating the level crossing rate. This method requires knowledge of the channel impulse response, as well as the derivatives of the real and imaginary components of it. Comparison of the analytical level crossing rate to measured results shows good agreement.

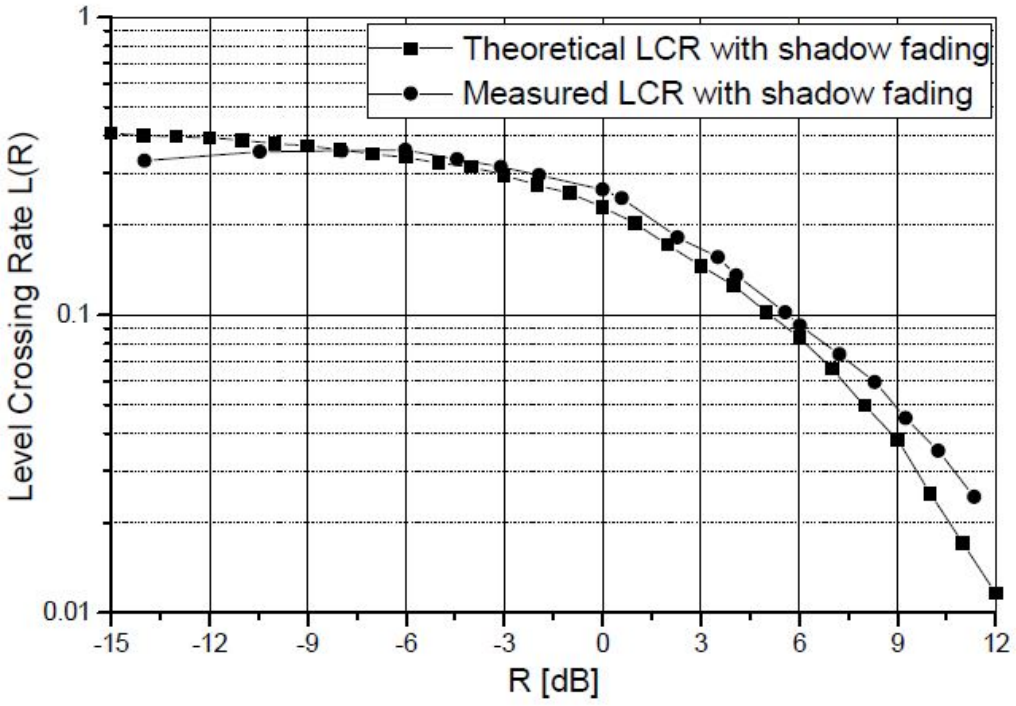

Figure 4.2: Theoretical and measured level crossing rates *with* shadow fading.

CHAPTER V

SIMULATOR

5.1 Overview

The simulation of UV-to-UV channels is an integral part of link layer simulations, as well as the overall characterization of system performance. The channel model discussed earlier is a useful mathematical tool to explain the propagation mechanisms, and also for the statistical characterization of the channel. This model is impractical for simulators though, due to its assumption of an infinite number of scatterers [28]. This section describes a simulation model with a finite number of scatterers, which still matches the statistical properties of the reference model. This simulator can be used to accurately represent the underwater channel of interest for research purposes.

5.2 Simulator for frequency-flat UV-to-UV Acoustic Fading Channel

If a SWA isovelocity environment is assumed, the frequency-flat complex faded envelope can be written as $h(t) = h^{LoS}(t) + h^{UA}(t) + h^{DA}(t)$ where

$$h^{LoS}(t) = \sqrt{\frac{K}{K+1}} e^{j2\pi t[f_{\mathrm{Tmax}}\cos(\alpha_{TR}+\pi-\gamma_T)+f_{\mathrm{Rmax}}\cos(\alpha_{TR}-\gamma_R)]} \tag{5.1}$$

$$\begin{aligned} h^{UA}(t) &= \sqrt{\frac{\eta_B}{2B(K+1)}} \sum_{b=1}^{B} \sum_{\hat{s}=b-1}^{b} \sqrt{\frac{1}{M_{b\hat{s}}}} \sum_{m=1}^{M_{b\hat{s}}} e^{j\phi_{b\hat{s}m}} \\ &\times e^{j2\pi t\left(\frac{1}{\lambda t}\Delta Z_{b\hat{s}m}(t)\sin\alpha_{Rb\hat{s}m}+f_{\mathrm{Tmax}}\cos(3\pi-\alpha_{Rb\hat{s}m}-\gamma_T)+f_{\mathrm{Rmax}}\cos(\alpha_{Rb\hat{s}m}-\gamma_R)\right)} \end{aligned} \tag{5.2}$$

$$\begin{aligned} h^{DA}(t) &= \sqrt{\frac{\eta_S}{2S(K+1)}} \sum_{s=1}^{S} \sum_{\hat{b}=s-1}^{s} \sqrt{\frac{1}{N_{s\hat{b}}}} \sum_{n=1}^{N_{s\hat{b}}} e^{j\phi_{s\hat{b}n}} \\ &\times e^{j2\pi t\left(\frac{1}{\lambda t}\Delta Z_{s\hat{b}n}(t)\sin\alpha_{Rs\hat{b}n}+f_{\mathrm{Tmax}}\cos(\pi-\alpha_{Rs\hat{b}n}-\gamma_T)+f_{\mathrm{Rmax}}\cos(\alpha_{Rs\hat{b}n}-\gamma_R)\right)} \end{aligned} \tag{5.3}$$

In this model, the angles of arrival $\alpha_{Rb\hat{s}m}$ and $\alpha_{Rs\hat{b}n}$ are modeled using the Gaussian pdfs from (3.14) and (3.15) and are created as follows:

$$\alpha_{Rb\hat{s}m} = F^{-1}\left(\frac{m+0.1}{0.5\cdot M_{b\hat{s}}}, \mu_{UAb\hat{s}}, \sigma_{UAb\hat{s}}\right), \tag{5.4}$$

$$\alpha_{Rs\hat{b}n} = F^{-1}\left(\frac{n+0.1}{0.9\cdot N_{s\hat{b}}}, \mu_{DAs\hat{b}}, \sigma_{DAs\hat{b}}\right) \tag{5.5}$$

for $m = 0, 0.5, 1, \ldots, M_{b\hat{s}}/2$, $n = 0, 0.5, 1 \ldots, N_{s\hat{b}}/2$, where $F(\ \cdot\ )^{-1}$ denotes the inverse cumulative Gaussian distribution function. The surface displacements $Z_{b\hat{s}m}(t)$ and $Z_{s\hat{b}n}(t)$ are modeled using Gaussian pdfs from (3.16) and (3.17), and are generated as follows:

$$Z_{b\hat{s}m}(t) = F^{-1}\left(\frac{m+0.1}{1.8\cdot M_{b\hat{s}}}, 0, \zeta_{\Delta Z_{UAb\hat{s}}}\right), \tag{5.6}$$

$$Z_{s\hat{b}n}(t) = F^{-1}\left(\frac{n+0.1}{2.1\cdot N_{s\hat{b}}}, 0, \zeta_{\Delta Z_{DAs\hat{b}}}\right), \tag{5.7}$$

for $m = 0, 0.5, 1, \ldots, M_{b\hat{s}}/2$, $n = 0, 0.5, 1 \ldots, N_{s\hat{b}}/2$, where $F(\ \cdot\ )^{-1}$ denotes the inverse cumulative Gaussian distribution function. The phases $\phi_{b\hat{s}m}$ and $\phi_{s\hat{b}n}$ are generated as independent uniform random variables on the interval $[-\pi, \pi)$.

5.3 Simulation Results

To verify the proposed simulation model, the simulation model is compared with the reference model described earlier. Fig. 5.1 compares the simulated temporal correlation functions with the theoretical temporal correlation functions. The theoretical and simulated curves in Fig. 5.1 are obtained with the central frequency $f_c = 17$ kHz and the parameters $c = 1470$ m/s, $R = 5$ km, $h = 20$ m, $h_T = 19$ m, $h_R = 18$ m, $K = 0.8$, $S = B = 1$, $v_T = 0.0006$ m/s, $v_R = 0.00025$ m/s, $\mu_{DA10} = 166.5°$, $\mu_{DA11} = 169°$, $\mu_{UA10} = 194.9°$, $\mu_{UA11} = 195.9°$, $\sigma_{DA10} = 3.25°$, $\sigma_{DA11} = 5°$, $\sigma_{UA10} = 2.7°$, $\sigma_{UA11} = 3.2°$, $\zeta_{\Delta Z_{DA10}} = \zeta_{\Delta Z_{DA11}} 0.0097$, $\zeta_{\Delta Z_{UA10}} = \zeta_{\Delta Z_{UA11}} = 0.0087$, $\eta_B = 0.28$, and $\eta_S = 1 - \eta_B$. It is assumed that the T_x and R_x are relatively stationary, i.e., slightly moving with waves (i.e.,

$\gamma_T = \gamma_R = 90°$). Finally, the number of scatterers in the simulator is set to $M_{b\hat{s}} = 10$ and $N_{s\hat{b}} = 10$. A good match can be observed between theoretical and simulated curves. An even better match can be obtained by simulating with a larger numbers of scatterers, but at a cost of proportionally longer simulation times.

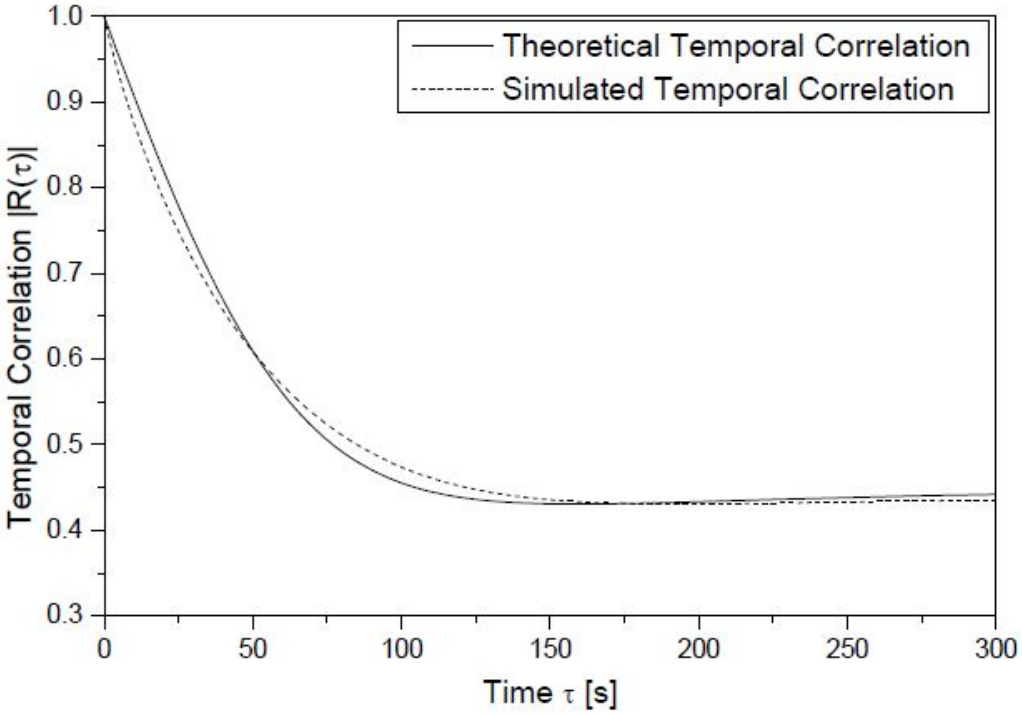

Figure 5.1: The magnitudes of simulated and theoretical temporal correlation functions.

5.4 Summary

A simulator for the underwater acoustic fading channel is proposed in this chapter. The simulator employs a finite number of scatterers in order to model the signal propagation through the channel, while still maintaining the statistical properties of the reference model. A time variant transfer function is proposed, which is the frequency domain version of the channel impulse response. The simulated results agree well with the theoretical model.

CHAPTER VI

VELOCITY ESTIMATOR

6.1 Overview

In this section, closed-form expressions for the joint estimation of the velocities of the T_x and R_x are developed. A practical estimation algorithm is also proposed, which guarantees non-negative non-complex estimated velocities. The expressions for the velocities are derived under the assumption of a noise-free isotropic scattering environment with no LoS component. The transmitter and receiver velocities v_t and v_r are proportional to the maximum Doppler angular frequencies w_t and w_r respectively, so the following work will focus on the estimation w_t and w_r to help simplify the notation.

The transmitter and receiver angular frequencies w_{Tmax} and w_{Rmax} are estimated by combining the number of zero-crossings with the number of maxima in the in-phase or real component and quadrature or imaginary component of $h(t)$. These are labeled $h_i(t)$ and $h_q(t)$ respectively. These components of $h(t)$ are observed over a length of time T. This crossing-based estimation approach was chosen because it does not depend on the type of propagation environment. Derivatives of the autocorrelation function are calculated to obtain the level-crossing rate and number of maxima during a specified time interval. These parameters are then used to solve for the angular frequencies, from which the velocities can be extracted.

The remainder of this chapter is organized as follows. Section 6.2 derives an expression for the level crossing rate in terms of the angular frequencies of the transmitter and receiver. Section 6.3 derives an expression for the number of maxima in the channel, also in terms of the angular frequencies of the transmitter

and receiver. Section 6.4 combines these expressions to develop expressions for the angular frequencies in terms of the LCR and number of maxima. Section 6.5 calculates the root mean square error of the frequencies for a variety of parameters, and graphs the results. Finally, section 6.6 contains some concluding comments.

6.2 Level-Crossing Rate

The upward arriving autocorrelation function defined as in 3.32 is rewritten as

$$R^{UA}(\tau) \;=\; \frac{\eta_B}{2B(K+1)} \sum_{b=1}^{B} \sum_{\hat{s}=b-1}^{b} e^{\tau(a_{UAb\hat{s}}+jb_{UAb\hat{s}})} e^{\tau^2 c_{UAb\hat{s}}}, \tag{6.1}$$

where $a_{UAb\hat{s}}$, $b_{UAb\hat{s}}$, and $c_{UAb\hat{s}}$ are defined in 4.14–4.16, with the corresponding downward arriving elements defined similarly.

The level crossing rate $L_{h_i}(0,T)$ is defined here as the number of times that the in-phase component $h_i(t)$ crosses the zero-level threshold with a positive slope over the time interval $(0,T]$. Similarly, $L_{h_q}(0,T)$ defines the number of positive-slope zero-crossings for the quadrature component $h_q(t)$ over the same interval.

As noted in 4.2, the level-crossing rate can be calculated by obtaining the expressions for the b_n values [18],

$$b_0 \;\triangleq\; \mathrm{E}[h_i(t)^2] = \mathrm{E}[h_q(t)^2], \tag{6.2}$$

$$b_2 \;\triangleq\; \mathrm{E}[\dot{h}_i(t)^2] = \mathrm{E}[\dot{h}_q(t)^2], \tag{6.3}$$

$$b_4 \;\triangleq\; \mathrm{E}[\ddot{h}_i(t)^2] = \mathrm{E}[\ddot{h}_q(t)^2], \tag{6.4}$$

and b_2 is found from 4.15 to be [27]

$$b_2^{UA} \;=\; \frac{b_0^{UA}}{2B} \sum_{b=1}^{B} \sum_{\hat{s}=b-1}^{b} b_{UAb\hat{s}}^2 - a_{UAb\hat{s}}^2 + 2c_{UAb\hat{s}}. \tag{6.5}$$

Some assumptions about the channel are made here for ease in calculation. It is assumed that $\mu_{UAb\hat{s}} = 180^\circ$ and that $\sigma_{UAb\hat{s}} = 1$. With these assumptions in place,

the above parameters can be rewritten as:

$$a_{UAb\hat{s}} = 0, \tag{6.6}$$

$$b_{UAb\hat{s}} = -2\pi\Big[f_{\mathrm{Rmax}}\cos(\gamma_R) + f_{\mathrm{Tmax}}\cos(\gamma_T)\Big], \tag{6.7}$$

$$c_{UAb\hat{s}} = \frac{1}{2}\Big[2\pi f_{\mathrm{Rmax}}\sin(\gamma_R) + 2\pi f_{\mathrm{Tmax}}\sin(\gamma_T)\Big]^2, \tag{6.8}$$

This will then lead to

$$\begin{aligned} b_2^{UA} &= \frac{b_0^{UA}}{2B}\sum_{b=1}^{B}\sum_{\hat{s}=b-1}^{b}\Big[2\pi f_{\mathrm{Tmax}}\cos(\gamma_T) - 2\pi f_{\mathrm{Rmax}}\cos(\gamma_R)\Big]^2 \\ &+ \Big[2\pi f_{\mathrm{Tmax}}\sin(\gamma_T) + 2\pi f_{\mathrm{Rmax}}\sin(\gamma_R)\Big]^2, \end{aligned} \tag{6.9}$$

Expanding yields:

$$\begin{aligned} b_2^{UA} &= b_0^{UA}(2\pi)^2\Big[f_{\mathrm{Tmax}}^2\cos^2(\gamma_T) - 2f_{\mathrm{Tmax}}f_{\mathrm{Rmax}}\cos(\gamma_T)\cos(\gamma_R) + f_{\mathrm{Rmax}}^2\cos^2(\gamma_R) \\ &+ f_{\mathrm{Tmax}}^2\sin^2(\gamma_T) + 2f_{\mathrm{Tmax}}f_{\mathrm{Rmax}}\sin(\gamma_T)\sin(\gamma_R) + f_{\mathrm{Rmax}}^2\sin^2(\gamma_R)\Big]. \end{aligned} \tag{6.10}$$

After collecting similar terms, the trigonometric identities $\cos(x)^2+\sin(x)^2=1$ and $\cos(a+b)=\cos(a)\cos(b)$-$\sin(a)\sin(b)$ can be used to give

$$b_2^{UA} = b_0^{UA}(2\pi)^2\Big[f_{\mathrm{Tmax}}^2 - 2f_{\mathrm{Tmax}}f_{\mathrm{Rmax}}\cos(\gamma_T+\gamma_R) + f_{\mathrm{Rmax}}^2\Big]. \tag{6.11}$$

The dependence between velocity and direction angles is removed by treating γ_T and γ_R as random variables, with all directions being equally probable. These variables then have a uniform distribution over the interval $[0, 2\pi]$. By averaging over all possible values of γ_T and γ_R, the cosine term goes to zero, leaving

$$b_2^{UA} = b_0^{UA}(2\pi)^2[f_{\mathrm{Tmax}}^2 + f_{\mathrm{Rmax}}^2], \tag{6.12}$$

and combining with the DA component will give the result

$$b_2 = b_0(2\pi)^2[f_{\mathrm{Tmax}}^2 + f_{\mathrm{Rmax}}^2], \tag{6.13}$$

which will be used to help estimate the velocity. For stationary zero-mean Gaussian processes, the number of zero crossings can be written as [26]

$$E[L] = \frac{T}{2\pi}\sqrt{\frac{b_2}{b_0}}, \tag{6.14}$$

or

$$E[L] = \frac{T}{2\pi}\sqrt{w_{\mathrm{Tmax}}^2 + w_{\mathrm{Rmax}}^2}, \tag{6.15}$$

6.3 Number of Maxima

The number of maxima is defined here as $M_{h_i}(T)$ for the in-phase component during the time interval $(0, T]$, while $M_{h_q}(T)$ is the number of maxima of the quadrature component. The b_4 term described in the previous section is found by taking half the real component of the fourth derivative of 6.1. This results in the expression

$$\begin{aligned} b_4^{UA} &= \Re\left\{\frac{1}{2}\frac{d^4R^{UA}(\tau)}{d\tau^4}_{\tau=0}\right\} \\ &= \frac{b_0^{UA}}{2B}\sum_{b=1}^{B}\sum_{\hat{s}=b-1}^{b}\frac{1}{2}a_{UAb\hat{s}}^4 - 3a_{UAb\hat{s}}^2 b_{UAb\hat{s}}^2 - 6a_{UAb\hat{s}}^2 c_{UAb\hat{s}} \\ &+ \frac{1}{2}b_{UAb\hat{s}}^4 + 6b_{UAb\hat{s}}^2 c_{UAb\hat{s}} + 6c_{UAb\hat{s}}^2. \end{aligned} \tag{6.16}$$

When applying the simplifications from the previous section, this becomes

$$b_4^{UA} = \frac{b_0^{UA}}{2B}\sum_{b=1}^{B}\sum_{\hat{s}=b-1}^{b}\frac{1}{2}b_{UAb\hat{s}}^4 + 6b_{UAb\hat{s}}^2 c_{UAb\hat{s}} + 6c_{UAb\hat{s}}^2. \tag{6.17}$$

Filling in the terms will give

$$\begin{aligned} b_4^{UA} &= b_0^{UA}(2\pi)^4\left[\frac{1}{2}\left(f_{\mathrm{Tmax}}\cos(\gamma_T) - f_{\mathrm{Rmax}}\cos(\gamma_R)\right)^4\right. \\ &- 3\left(f_{\mathrm{Tmax}}\cos(\gamma_T) - f_{\mathrm{Rmax}}\cos(\gamma_R)\right)^2\left(f_{\mathrm{Tmax}}\sin(\gamma_T) - f_{\mathrm{Rmax}}\sin(\gamma_R)\right)^2 \\ &+ \left.\frac{6}{4}\left(f_{\mathrm{Tmax}}\sin(\gamma_T) + f_{\mathrm{Rmax}}\sin(\gamma_R)\right)^4\right], \end{aligned} \tag{6.18}$$

and expanding these terms gives

$$\begin{aligned}
b_4^{UA} &= b_0^{UA}(2\pi)^4\Bigg[\frac{1}{2}f_{\mathrm{Tmax}}^4\cos^4(\gamma_T)+\frac{1}{2}f_{\mathrm{Rmax}}^4\cos^4(\gamma_R)-2f_{\mathrm{Tmax}}^3f_{\mathrm{Rmax}}\cos^3(\gamma_T)\cos(\gamma_R)\\
&- 2f_{\mathrm{Tmax}}f_{\mathrm{Rmax}}^3\cos(\gamma_T)\cos^3(\gamma_R)+3f_{\mathrm{Tmax}}^2f_{\mathrm{Rmax}}^2\cos^2(\gamma_T)\cos^2(\gamma_R)\\
&+ 3\Bigg\{(f_{\mathrm{Tmax}}^4\sin^2(\gamma_T)\cos^2(\gamma_T)+f_{\mathrm{Rmax}}^4\sin^2(\gamma_R)\cos^2(\gamma_R)\\
&+ 2f_{\mathrm{Tmax}}^3f_{\mathrm{Rmax}}\cos^2(\gamma_T)\sin(\gamma_T)\sin(\gamma_R)+2f_{\mathrm{Tmax}}f_{\mathrm{Rmax}}^3\cos^2(\gamma_R)\sin(\gamma_T)\sin(\gamma_R)\\
&- 2f_{\mathrm{Tmax}}^3f_{\mathrm{Rmax}}\cos(\gamma_T)\sin^2(\gamma_T)\cos(\gamma_R)-2f_{\mathrm{Tmax}}f_{\mathrm{Rmax}}^3\cos(\gamma_T)\cos(\gamma_R)\sin^2(\gamma_R)\\
&+ f_{\mathrm{Tmax}}^2f_{\mathrm{Rmax}}^2\cos^2(\gamma_T)\sin^2(\gamma_R)+f_{\mathrm{Tmax}}^2f_{\mathrm{Rmax}}^2\cos^2(\gamma_R)\sin^2(\gamma_T)\\
&- 4f_{\mathrm{Tmax}}^2f_{\mathrm{Rmax}}^2\cos(\gamma_T)\sin(\gamma_T)\cos(\gamma_R)\sin(\gamma_R)\Bigg\}\\
&+ \frac{3}{2}f_{\mathrm{Tmax}}^4\sin^4(\gamma_T)+\frac{3}{2}f_{\mathrm{Rmax}}^4\sin^4(\gamma_R)+9f_{\mathrm{Tmax}}^2f_{\mathrm{Rmax}}^2\sin^2(\gamma_T)\sin^2(\gamma_R)\\
&+ 6f_{\mathrm{Tmax}}^3f_{\mathrm{Rmax}}\sin^3(\gamma_T)\sin(\gamma_R)+6f_{\mathrm{Tmax}}f_{\mathrm{Rmax}}^3\sin(\gamma_T)\sin^3(\gamma_R)\Bigg]. \qquad (6.19)
\end{aligned}$$

Again treating γ_T and γ_R as random variables, this expression can be greatly simplified to

$$\begin{aligned}
b_4^{UA} &= b_0^{UA}(2\pi)^4\Bigg[\frac{3}{16}f_{\mathrm{Tmax}}^4+\frac{3}{16}f_{\mathrm{Rmax}}^4+\frac{3}{4}f_{\mathrm{Tmax}}^2f_{\mathrm{Rmax}}^2\\
&+ \frac{3}{8}f_{\mathrm{Tmax}}^4+\frac{3}{8}f_{\mathrm{Rmax}}^4+\frac{3}{4}f_{\mathrm{Tmax}}^2f_{\mathrm{Rmax}}^2+\frac{3}{4}f_{\mathrm{Tmax}}^2f_{\mathrm{Rmax}}^2\\
&+ \frac{9}{16}f_{\mathrm{Tmax}}^4+\frac{9}{16}f_{\mathrm{Rmax}}^4+\frac{9}{4}f_{\mathrm{Tmax}}^2f_{\mathrm{Rmax}}^2\Bigg], \qquad (6.20)
\end{aligned}$$

and like terms can be gathered to leave

$$b_4^{UA} = b_0^{UA}(2\pi)^4\left[\frac{9}{8}f_{\mathrm{Tmax}}^4+\frac{9}{8}f_{\mathrm{Rmax}}^4+\frac{9}{2}f_{\mathrm{Tmax}}^2f_{\mathrm{Rmax}}^2\right], \qquad (6.21)$$

and combining with the DA component gives

$$b_4 = b_0(2\pi)^4\left[\frac{9}{8}f_{\mathrm{Tmax}}^4+\frac{9}{8}f_{\mathrm{Rmax}}^4+\frac{9}{2}f_{\mathrm{Tmax}}^2f_{\mathrm{Rmax}}^2\right], \qquad (6.22)$$

For stationary zero-mean Gaussian processes, the number of maxima can be written as [26]

$$E[M] = \frac{T}{2\pi}\sqrt{\frac{b_4}{b_2}}, \qquad (6.23)$$

or

$$E[M] = \frac{T}{2\pi}\sqrt{\frac{\frac{9}{8}w_{\mathrm{Tmax}}^4 + \frac{9}{8}w_{\mathrm{Rmax}}^4 + \frac{9}{2}w_{\mathrm{Tmax}}^2 w_{\mathrm{Rmax}}^2}{w_{\mathrm{Tmax}}^2 + w_{\mathrm{Rmax}}^2}}, \tag{6.24}$$

6.4 Estimation of Velocity

The velocities of the transmitter and receiver can be obtained from 6.15 and 6.24, by solving for w_{Tmax} and w_{Rmax}. By rearranging 6.15, it becomes

$$(\frac{2\pi}{T})^2 L^2 = w_{\mathrm{Tmax}}^2 + w_{\mathrm{Rmax}}^2, \tag{6.25}$$

and inserting this into 6.24 gives

$$M = \frac{T}{2\pi}\sqrt{\frac{\frac{9}{8}w_{\mathrm{Tmax}}^4 + \frac{9}{8}w_{\mathrm{Rmax}}^4 + \frac{9}{2}w_{\mathrm{Tmax}}^2 w_{\mathrm{Rmax}}^2}{(\frac{2\pi}{T})^2 L^2}}, \tag{6.26}$$

and rearranging terms yields

$$(\frac{2\pi}{T})^2 M^2 (\frac{2\pi}{T})^2 L^2 = \frac{9}{8}w_{\mathrm{Tmax}}^4 + \frac{9}{8}w_{\mathrm{Rmax}}^4 + \frac{9}{2}w_{\mathrm{Tmax}}^2 w_{\mathrm{Rmax}}^2. \tag{6.27}$$

At this point, either w_{Tmax} or w_{Rmax} can be solved for. For this derivation, w_{Tmax} is chosen.

$$\begin{aligned}
(\frac{2\pi}{T})^4 M^2 L^2 &= \frac{9}{8}(w_{\mathrm{Tmax}}^4 + w_{\mathrm{Rmax}}^4) + \frac{9}{2}w_{\mathrm{Tmax}}^2 w_{\mathrm{Rmax}}^2 \\
&= \frac{9}{8}(w_{\mathrm{Tmax}}^2 + w_{\mathrm{Rmax}}^2)^2 - (\frac{9}{4} - \frac{9}{2})w_{\mathrm{Tmax}}^2 w_{\mathrm{Rmax}}^2 \\
&= \frac{9}{8}(\frac{2\pi}{T})^4 L^4 + \frac{9}{4}w_{\mathrm{Tmax}}^2\left((\frac{2\pi}{T})^2 L^2 - w_{\mathrm{Tmax}}^2\right).
\end{aligned} \tag{6.28}$$

Next, all terms are moved to one side of the equation, and the quadratic equation is used to solve for w_{Tmax}^2

$$\begin{aligned}
0 &= \frac{9}{8}(\frac{2\pi}{T})^4 L^4 + \frac{9}{4}w_{\mathrm{Tmax}}^2\left((\frac{2\pi}{T})^2 L^2 - w_{\mathrm{Tmax}}^2\right) - (\frac{2\pi}{T})^4 M^2 L^2 \\
&= -\frac{9}{4}w_{\mathrm{Tmax}}^4 + \frac{9}{4}w_{\mathrm{Tmax}}^2(\frac{2\pi}{T})^2 L^2 + \frac{9}{8}(\frac{2\pi}{T})^4 L^4 - (\frac{2\pi}{T})^4 M^2 L^2 \\
&= w_{\mathrm{Tmax}}^4 - w_{\mathrm{Tmax}}^2(\frac{2\pi}{T})^2 L^2 - \frac{1}{2}(\frac{2\pi}{T})^4 L^4 + \frac{4}{9}(\frac{2\pi}{T})^4 M^2 L^2.
\end{aligned} \tag{6.29}$$

$$w_{\mathrm{Tmax}}^2 = \frac{(\frac{2\pi L}{T})^2 \pm \sqrt{(\frac{2\pi L}{T})^4 - 4(-\frac{1}{2}(\frac{2\pi L}{T})^4 + \frac{4}{9}(\frac{2\pi}{T})^4 M^2 L^2)}}{2}$$
$$= \frac{(\frac{2\pi L}{T})^2 \pm \sqrt{3(\frac{2\pi L}{T})^4 - \frac{16}{9}(\frac{2\pi}{T})^4 M^2 L^2)}}{2}. \quad (6.30)$$

When implementing this estimator in Matlab, the number of zero crossings and the number of maxima were counted for both the real and the imaginary parts of the channel impulse response. This leads to four possible solutions for w_{Tmax}. The derivation for w_{Rmax} yields the same results. Empirical testing showed that the best results were obtained when

$$w_{\mathrm{Tmax1}} = \sqrt{\frac{(\frac{2\pi L_r}{T})^2 + \sqrt{3(\frac{2\pi L_r}{T})^4 - \frac{16}{9}(\frac{2\pi}{T})^4 M_r^2 L_r^2)}}{2}} \quad (6.31)$$

$$w_{\mathrm{Tmax2}} = \sqrt{\frac{(\frac{2\pi L_r}{T})^2 - \sqrt{3(\frac{2\pi L_r}{T})^4 - \frac{16}{9}(\frac{2\pi}{T})^4 M_r^2 L_r^2)}}{2}} \quad (6.32)$$

$$w_{\mathrm{Rmax1}} = \sqrt{\frac{(\frac{2\pi L_i}{T})^2 + \sqrt{3(\frac{2\pi L_i}{T})^4 - \frac{16}{9}(\frac{2\pi}{T})^4 M_i^2 L_i^2)}}{2}} \quad (6.33)$$

$$w_{\mathrm{Rmax2}} = \sqrt{\frac{(\frac{2\pi L_i}{T})^2 - \sqrt{3(\frac{2\pi L_i}{T})^4 - \frac{16}{9}(\frac{2\pi}{T})^4 M_i^2 L_i^2)}}{2}}, \quad (6.34)$$

and the final values for w_{Tmax} and w_{Rmax} are empirically determined to be

$$w_{\mathrm{Tmax}} = \min(\mathrm{abs}(w_{\mathrm{Tmax1}}), \mathrm{abs}(w_{\mathrm{Tmax2}})) \quad (6.35)$$

$$w_{\mathrm{Rmax}} = \min(\mathrm{abs}(w_{\mathrm{Rmax1}}), \mathrm{abs}(w_{\mathrm{Rmax2}})). \quad (6.36)$$

These values can both be divided by 2π to give

$$f_{\mathrm{Tmax}} = \min(\mathrm{abs}(f_{\mathrm{Tmax1}}), \mathrm{abs}(f_{\mathrm{Tmax2}})) \quad (6.37)$$

$$f_{\mathrm{Rmax}} = \min(\mathrm{abs}(f_{\mathrm{Rmax1}}), \mathrm{abs}(f_{\mathrm{Rmax2}})), \quad (6.38)$$

and the velocities can be calculated by using the relation $f = v/\lambda$

6.5 Evaluation of Velocity Estimator

The performance analysis of the proposed estimation algorithm is presented here. First, the root mean square error (RMSE) values are computed and plotted for the transmitter and receiver frequencies in a noise free environment with no LoS component. Next, the effects of LoS propagation, and changes in angle of arrival, surface displacement, angle spreads, and power distributions are measured. Finally, the effect of Gaussian noise on the estimator's performance is studied and reported. The estimation error for the velocities estimator is measured using the RMSE given by

$$\mathrm{E}[(\hat{f}_{T(R)} - f_{Tmax(Rmax)})^2]^{1/2} = \sqrt{\mathrm{Var}[\hat{f}_{T(R)}] + (\mathrm{E}[\hat{f}_{T(R)}] - f_{Tmax(Rmax)})^2} \tag{6.39}$$

where $\mathrm{Var}[\cdot]$ denotes the variance operation, $(\mathrm{E}[\hat{f}_{T(R)}] - f_{Tmax(Rmax)})^2$ represents the bias, and $\hat{f}_{T(R)} = \hat{w}_{T(R)}/(2\pi)$ and $f_{Tmax(Rmax)} = w_{Tmax(Rmax)}/(2\pi)$ denote the estimated and actual Doppler frequencies at the transmitter and receiver, respectively. Using the channel simulator developed earlier [28], with $M = 10$ and $N = 10$ scatterers at the ocean surface and bottom, 1,000 independent realizations of complex Gaussian processes are generated.

Fig. 6.1 shows the RMSE of the estimated transmitter Doppler frequency $\hat{f}_T$ versus the actual Doppler frequency f_{Tmax}, for several different receiver Doppler frequencies $f_{Rmax} = [0.01, 0.1, 1, 10, 25, 50]$ in a noise free isotropic scattering environment with no LoS component. The Doppler frequency is estimated for each iteration of the channel, and then all of the iterations are used to calculate the RMSE. Fig. 6.1 shows that the RMSE is higher for the smaller frequencies, usually around 40%, while at higher frequencies, it drops to about 30%.

Fig. 6.2 shows the RMSE of the estimated receiver Doppler frequency $\hat{f}_R$ versus the actual Doppler frequency f_{Rmax}, for several different transmitter Doppler

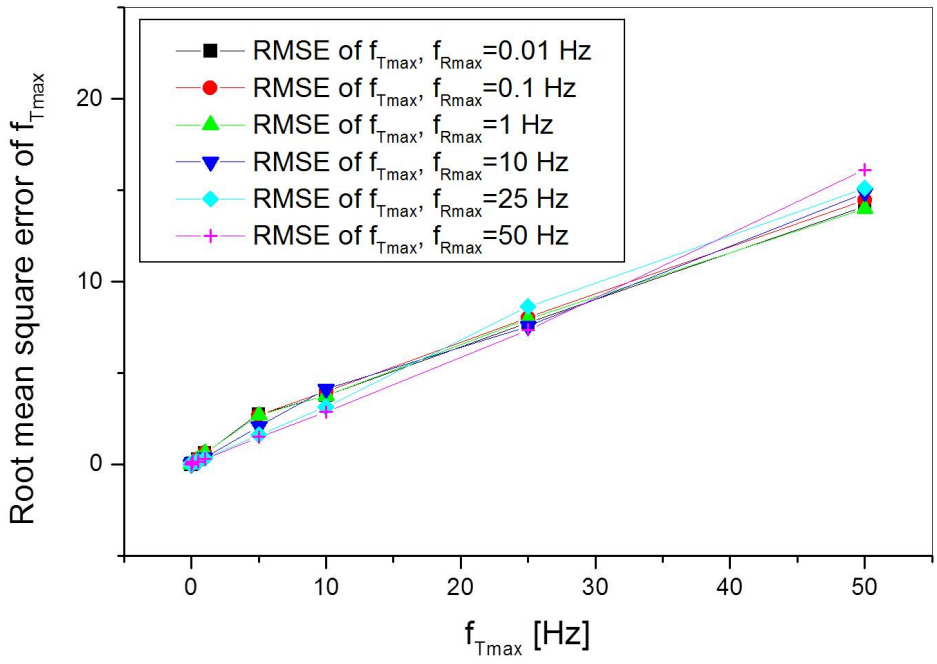

Figure 6.1: The RMSE of the estimated Doppler frequency $\hat{f}_T$ versus the actual Doppler frequency f_{Tmax} in a noise free isotropic scattering environment with no LoS component.

frequencies $f_{Tmax} = [0.01, 0.1, 1, 10, 25, 50]$ in a noise free isotropic scattering environment with no LoS component. The RMSE of the receiver is calculated in the same manner as the transmitter, and results show nearly identical errors.

Figs. 6.3- 6.5 shows the effect of the LoS component, the Ricean parameter K, on the performance of the proposed estimator. A noise free isotropic scattering environment is assumed, with $f_{Rmax} = f_{Tmax} = 0.1$ Hz,$f_{Rmax} = f_{Tmax} = 1$ Hz, and $f_{Rmax} = f_{Tmax} = 10$ Hz respectively. The results show that the RMSE for the transmitter and receiver are nearly identical, and are both rather high. Additionally, the error spikes when a LoS component is added, but remains fairly constant with increasing K.

Fig. 6.6 plots the RMSE of the estimated Doppler frequencies $\hat{f}_T$ and $\hat{f}_R$ versus the power distribution between the UA and DA rays. Interestingly, the error is highest

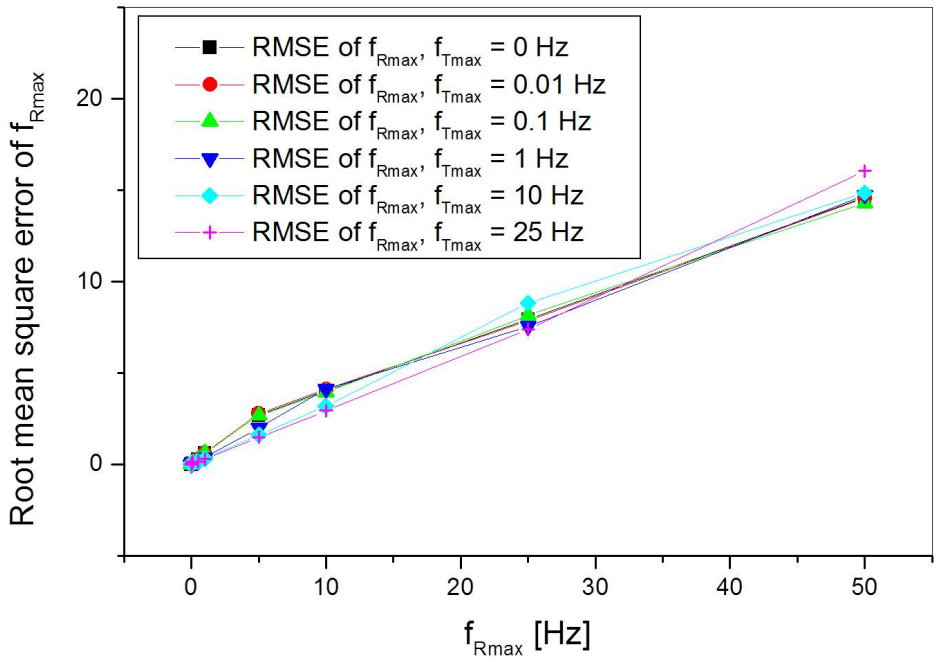

Figure 6.2: The RMSE of the estimated Doppler frequency $\hat{f}_R$ versus the actual Doppler frequency f_{Rmax} in a noise free isotropic scattering environment with no LoS component.

when the power is all in the UA component, and decreases as power shifts to the DA component.

The effect of non-isotropic scattering on the performance of the proposed estimator is examined next. The following plots show the effect of changes to various parameters in a noise free, non-isotropic scattering environment with no LoS component. Values of $f_{Rmax} = 2$ and $f_{Tmax} = 1$ were used for the simulations.

Figs. 6.7 and 6.8 plot the RMSE of the estimated Doppler frequencies $\hat{f}_T$ and $\hat{f}_R$ versus the mean angles of arrival. The error seems to be consistent, except when the UA and DA components are either 0 or 180 degrees.

Figs. 6.9 and 6.10 plot the RMSE of the estimated Doppler frequencies $\hat{f}_T$ and $\hat{f}_R$ versus the angle spreads. The error again seems to be constant, except when the UA and DA components are both 0 degrees, where there is a spike.

Figs. 6.11 and 6.12 plot the RMSE of the estimated Doppler frequencies $\hat{f}_T$ and $\hat{f}_R$ versus the vertical displacement of the ocean surface. The error seems to be fairly constant over all values.

Finally, the effect of white Gaussian noise on the proposed estimator is demonstrated. Fig. 6.13 shows the RMSE of the estimated transmitter Doppler frequency $\hat{f}_T$ versus the actual Doppler frequency f_{Tmax}, for several different receiver Doppler frequencies $f_{Rmax} = [0.01, 0.1, 1, 10, 25, 50]$ in a noise free isotropic scattering environment with no LoS component, while Fig. 6.14 shows the RMSE of the estimated receiver Doppler frequency $\hat{f}_R$ versus the actual Doppler frequency f_{Rmax}, for several different transmitter Doppler frequencies $f_{Tmax} = [0.01, 0.1, 1, 10, 25, 50]$ in a noise free isotropic scattering environment with no LoS component. The values were calculated for values of SNR = [5 10 15 20 25], but only the values for SNR = 10 are plotted here. The results show that the estimator performs similarly in the presence of this amount of noise than it did with a noise-free environment.

Overall, the results show a large degree of error introduced by each of the variables. This was expected to some degree due to the difficulty of the underwater propagation environment. However, with each variable adding anywhere from 20%–60% error, it appears that this estimator will not be feasible.

6.6 Summary

This chapter covers the derivation and development of the proposed velocity estimator. The level crossing rate for the shallow water acoustic channel was calculated, along with the number of maxima. The combination of these two expressions allowed for the angular frequency term to be isolated. The quadratic term led to two solutions each for the real and the imaginary components of the channel. Empirical testing led to expressions for calculating the frequency terms for

both transmitter and receiver. The estimator was tested, and the results show a rather high degree of error.

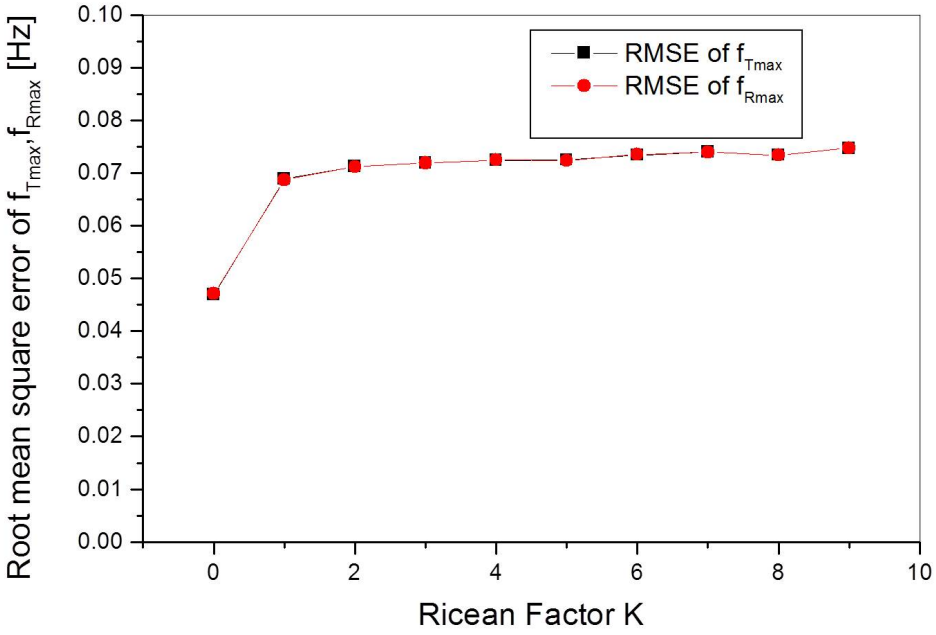

Figure 6.3: The RMSE of the estimated Doppler frequencies $\hat{f}_T$ and $\hat{f}_R$ versus Ricean factor K in a noise free isotropic scattering environment with a LoS component, for $f_{Rmax} = f_{Tmax} = 0.1$ Hz.

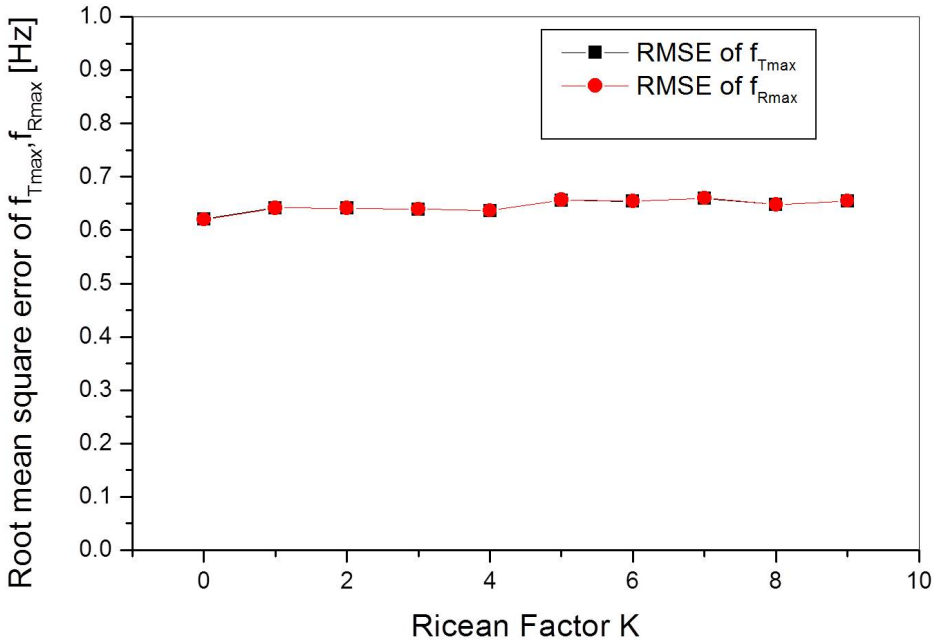

Figure 6.4: The RMSE of the estimated Doppler frequencies $\hat{f}_T$ and $\hat{f}_R$ versus Ricean factor K in a noise free isotropic scattering environment with a LoS component, for $f_{Rmax} = f_{Tmax} = 1$ Hz.

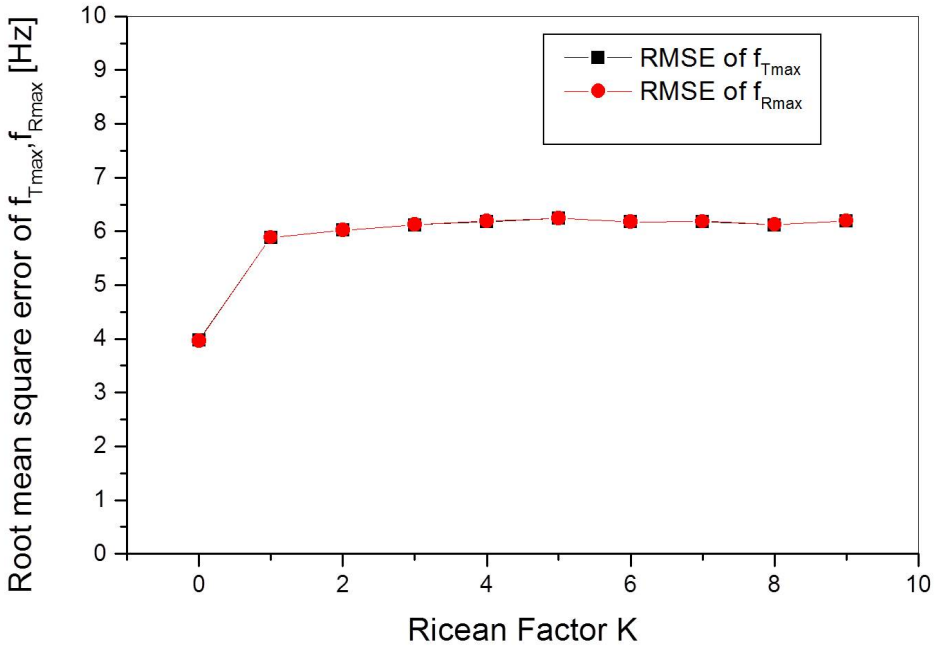

Figure 6.5: The RMSE of the estimated Doppler frequencies $\hat{f}_T$ and $\hat{f}_R$ versus Ricean factor K in a noise free isotropic scattering environment with a LoS component, for $f_{Rmax} = f_{Tmax} = 10$ Hz.

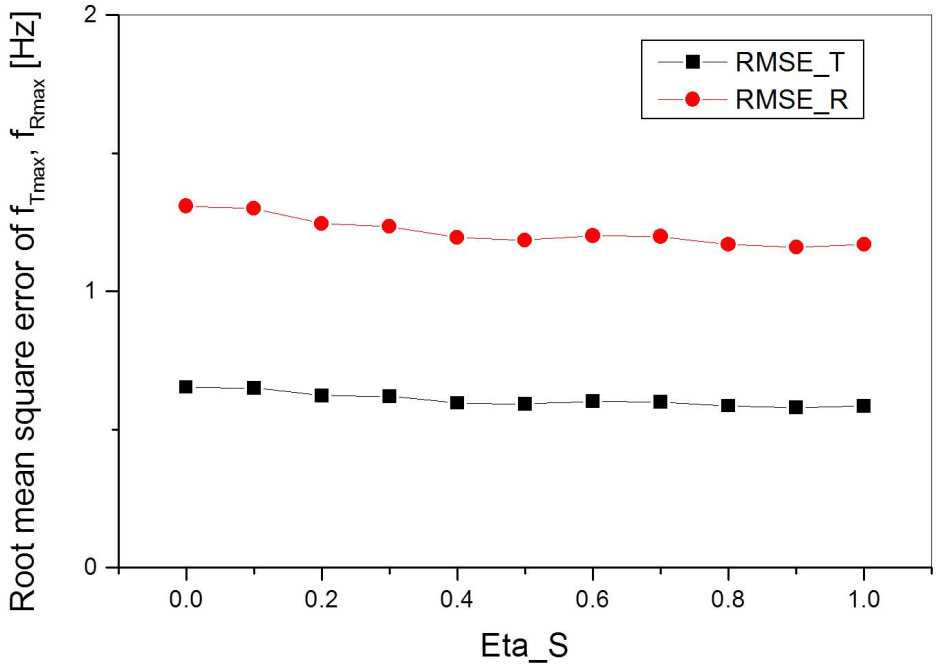

Figure 6.6: The RMSE of the estimated Doppler frequencies $\hat{f}_T$ and $\hat{f}_R$ versus the power distribution η in a noise free isotropic scattering environment with no LoS component.

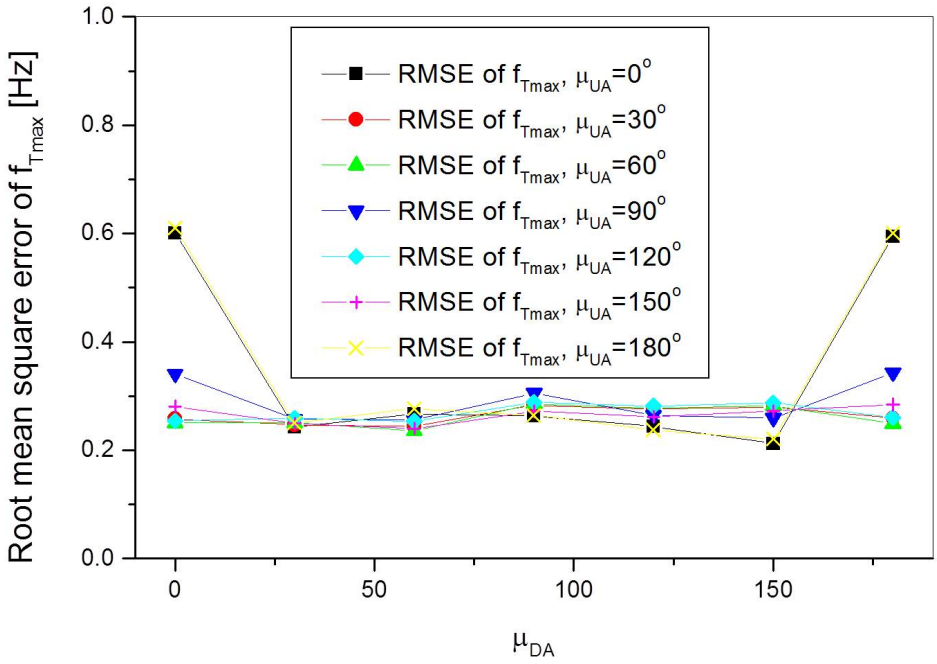

Figure 6.7: The RMSE of the estimated Doppler frequency $\hat{f}_T$ versus the mean angle of arrival μ in a noise free isotropic scattering environment with no LoS component.

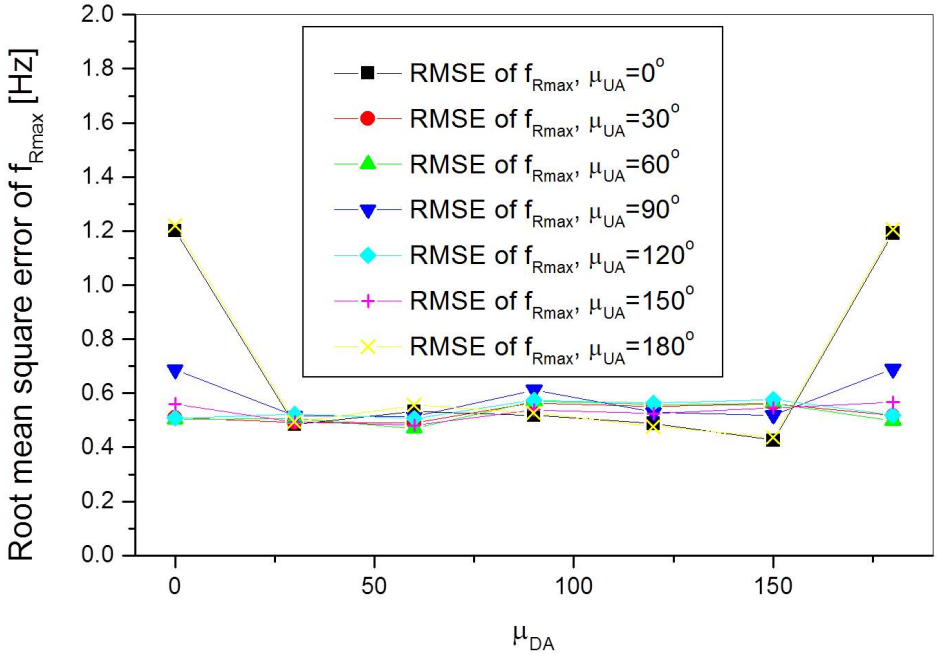

Figure 6.8: The RMSE of the estimated Doppler frequency $\hat{f}_R$ versus the mean angle of arrival μ in a noise free isotropic scattering environment with no LoS component.

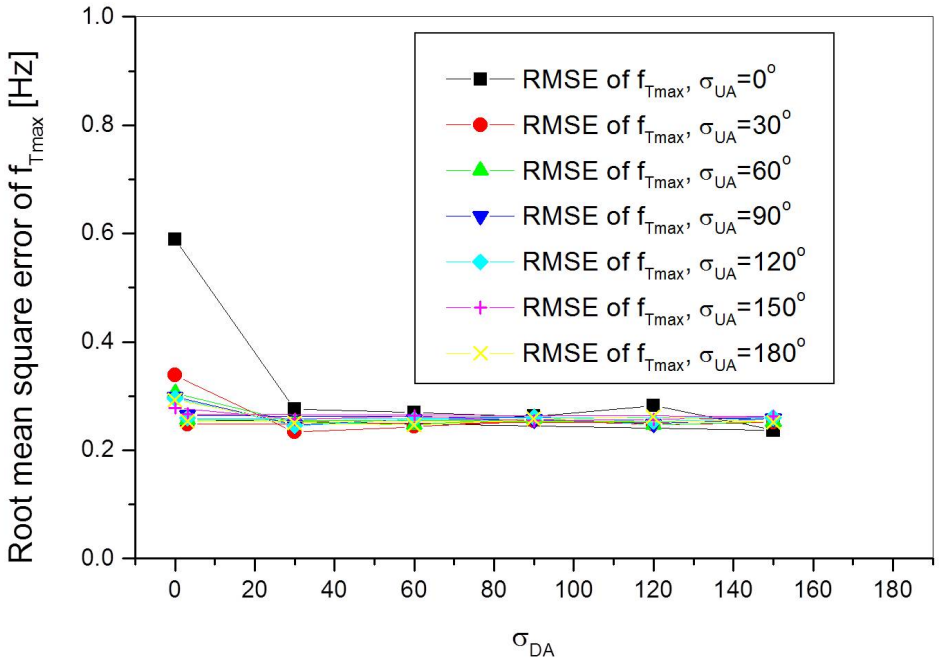

Figure 6.9: The RMSE of the estimated Doppler frequency $\hat{f}_T$ versus the angle spread σ in a noise free isotropic scattering environment with no LoS component.

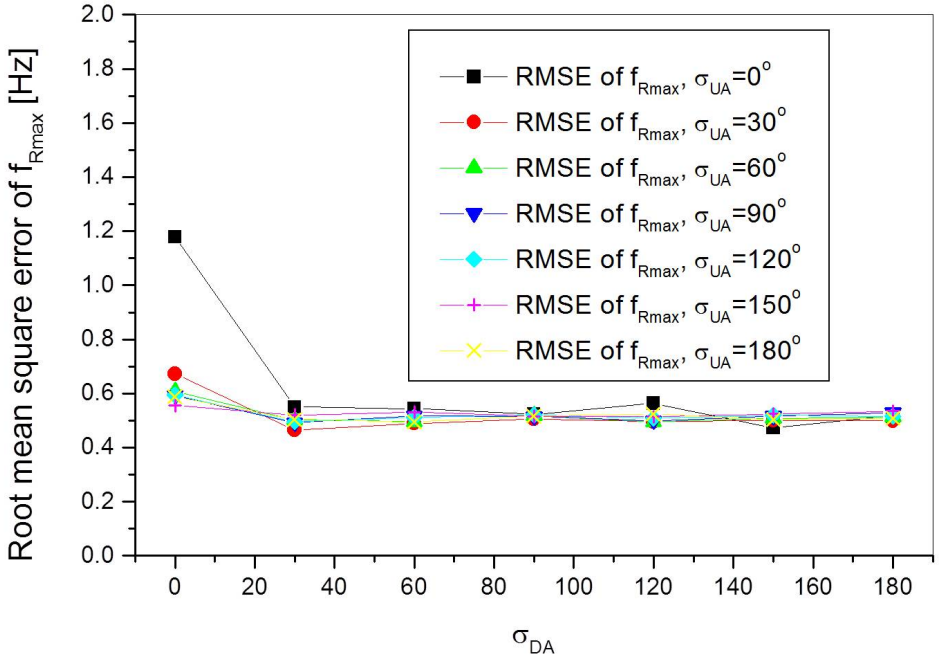

Figure 6.10: The RMSE of the estimated Doppler frequency $\hat{f}_R$ versus the angle spread σ in a noise free isotropic scattering environment with no LoS component.

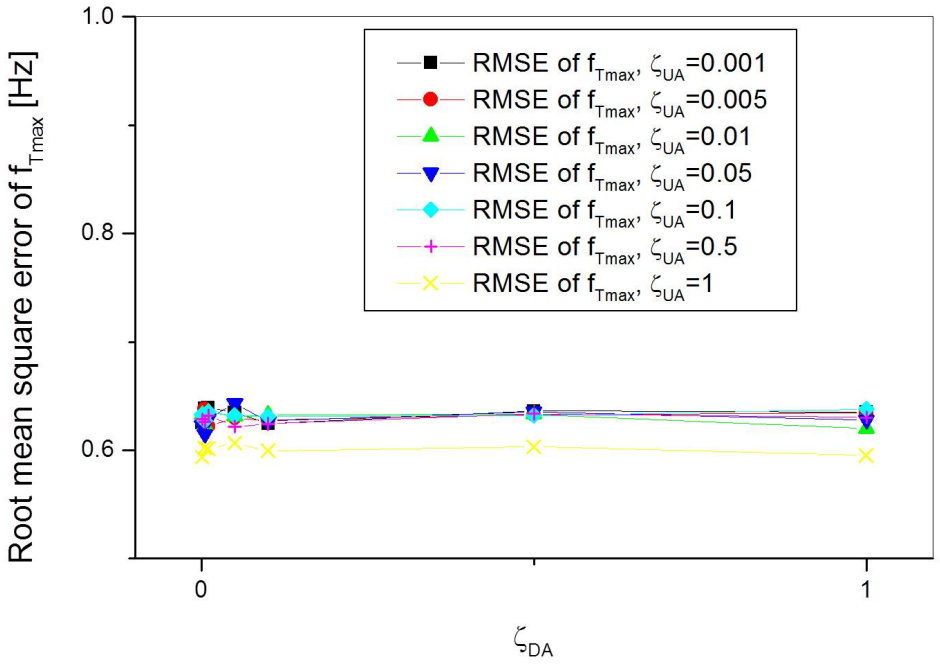

Figure 6.11: The RMSE of the estimated Doppler frequency $\hat{f}_T$ versus the vertical displacement of the ocean surface ζ in a noise free isotropic scattering environment with no LoS component.

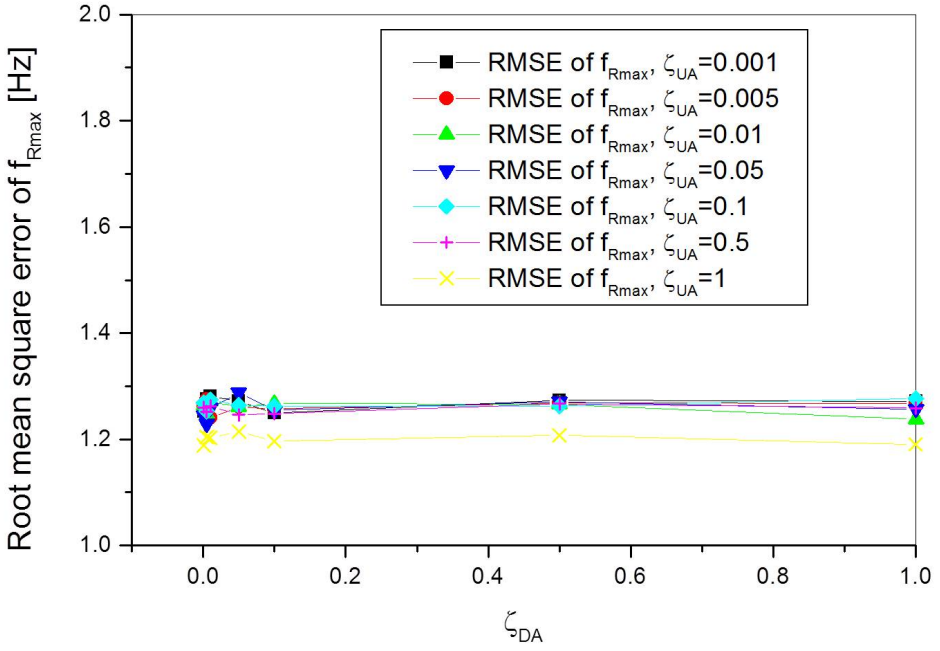

Figure 6.12: The RMSE of the estimated Doppler frequency $\hat{f}_R$ versus the vertical displacement of the ocean surface ζ in a noise free isotropic scattering environment with no LoS component.

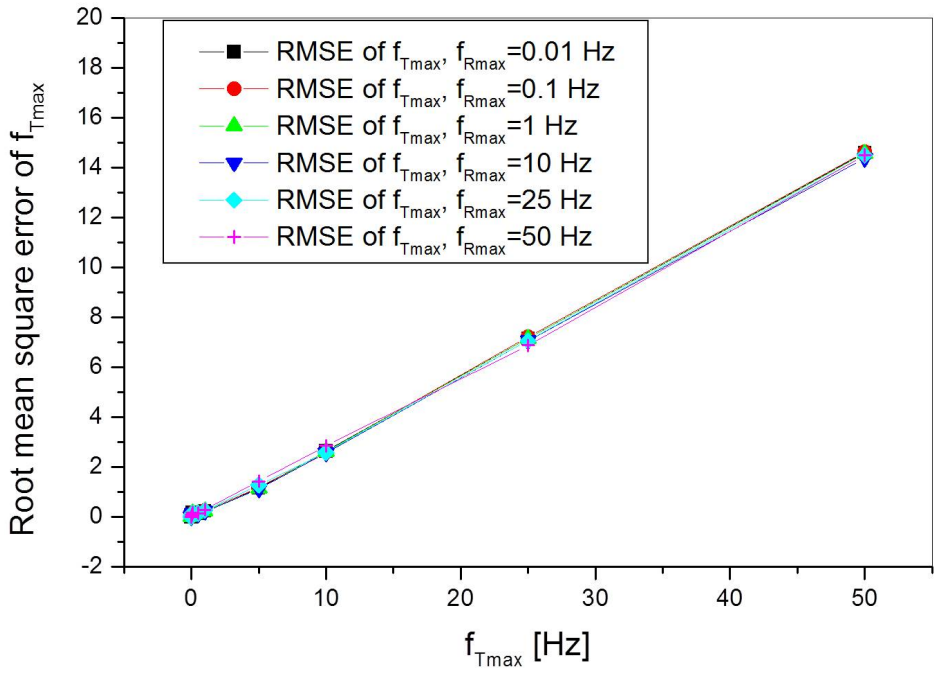

Figure 6.13: The RMSE of the estimated Doppler frequency $\hat{f}_T$ versus the actual Doppler frequency f_{Tmax} in a noise free isotropic scattering environment with no LoS component and with SNR=10dB.

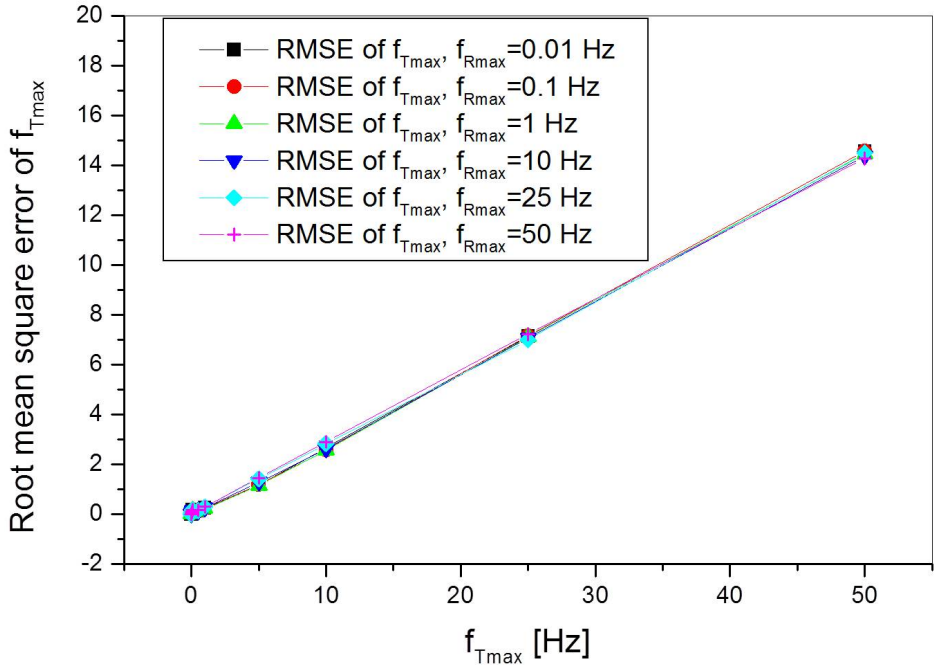

Figure 6.14: The RMSE of the estimated Doppler frequency $\hat{f}_R$ versus the actual Doppler frequency f_{Rmax} in a noise free isotropic scattering environment with no LoS component and with SNR=10dB.

CHAPTER VII

RESEARCH CONTRIBUTIONS AND FUTURE RESEARCH DIRECTIONS

7.1 Research Contributions

Underwater communications is a field with many potential applications that would benefit from better characterization of the environment. The contributions of this research is summarized as follows

- A method for calculating the level crossing rate of the shallow water acoustic channel was presented. The channel impulse response for the channel was derived, which utilized the principle of superposition to sum up all the reflected signals arriving at the receiver. The impulse response took into account random variables representing the angles of the rays, as well as variations in the ocean surface. The channel impulse response and its derivatives were used to calculate how often the signal crossed a specified threshold.

- A simulator for the underwater acoustic fading channel was proposed. The reference model describes an infinite number of scatterers and rays, making simulation unfeasible. The simulator instead uses a finite number of scatterers in order to model the signal propagation through the channel, while still maintaining the statistical properties of the reference model. The transfer function for the channel is derived, and used in the calculation of the autocorrelation function. The simulation results agree well with the theoretical predictions, and when more scatters are used in the simulation, a better match

is obtained. This better match comes at the cost of increased simulation time.

- A velocity estimator was developed for the shallow water environment. Expressions were derived for the level crossing rate and number of maxima in the real and imaginary parts of the channel. These expressions are used in combination to calculate the velocities of the transmitter and receiver.

7.2 Future Research Directions

An immediately apparent direction for future research efforts involves reducing or eliminating the bias in the calculations. This bias likely results from some of the assumptions made in the derivations of the channel impulse response and autocorrelation function. This bias prevents more accurate estimation of the velocity for this particular estimator. Preliminary efforts to reduce the error by estimating the bias and subtracting from the simulated frequencies were mostly unsuccessful. Another possibility for future work built on this research is to develop an estimator for the direction of movement of the transmitter and receiver. The estimation of direction should be possible using the estimated velocity, along with the cross correlation between the in-phase and quadrature components of the channel impulse response. However, preliminary research in this direction has not yet yielded feasible results.

Finally, another goal for future research would be developing the statistical characterization and framework for underwater channels other than the shallow water case. Developing a more general characterization of the underwater environment would be extremely valuable to the progress and utility of underwater communications applications.

REFERENCES

[1] Stojanovic M., "Acoustic (underwater) communications," *Encyclopedia of Telecommunications*, J. G. Proakis, Ed. John Wiley and Sons, 2003.

[2] Stojanovic M., "Recent advances in high-speed underwater acoustic communications," *IEEE Journal of Oceanic Engineering*, vol. 21, April 1996, pp. 125–136.

[3] Kilfoyle D. B. and A. B. Baggeroer, "The state of the art in underwater acoustic telemetry," *IEEE Journal of Oceanic Engineering*, vol. 25, January 2000, pp. 4–27.

[4] Catipovic J., "Performance limitations in underwater acoustic telemetry," *IEEE Journal of Oceanic Engineering*, vol. 15, July 1990, pp. 205-216.

[5] G. W. Elko, E. Diethorn, and T. Gänsler, "Room impulse response variation due to thermal fluctuation and its impact on acoustic echo cancellation," in Proc. Int. Workshop Acoust. Echo Noise Control, 2003, pp. 67-70.

[6] Brekhovskikh L. M. and Y. Lysanov, *Fundamentals of ocean acoustics 2e.* Springer, Berlin, 1991.

[7] Owen R. H., B. V. Smith, and R. F. W. Coates, "An experimental study of rough surface scattering and its effects on communication coherence," *MTS/IEEE Proceedings of OCEANS'94*, vol. 3, Brest, France, Sept. 1994, pp. 483–488.

[8] Essebbar A., G. Loubet, and F. Vial, "Underwater acoustic channel simulations for communication," *MTS/IEEE Proceedings of OCEANS'94*, vol. 3, Brest, France, Sept. 1994, pp. 495–500.

[9] Zielinski A., Y-H. Yoon, and L. Wu, "Performance analysis of digital acoustic communication in a shallow water channel," *IEEE Journal of Oceanic Engineering*, vol. 20, Oct. 1995, pp. 293–299.

[10] Bjerrum-Niese C., L. Bjorno, M. A. Pinto, and B. Quellec, "A simulation tool for high data-rate acoustic communication in a shallow-water, time-varying channel," *IEEE Journal of Oceanic Engineering*, vol. 21, Apr. 1996, pp. 143–149.

[11] Chitre M., "A high-frequency warm shallow water acoustic communications channel model and measurements," *Journal of the Acoustical Society of America*, vol. 122, Nov. 2007, pp. 2580–2586.

[12] Yang W. B. and T. C. Yang, "High-frequency channel characterization for M-ary frequency-shift-keying underwater acoustic communications," *Journal of the Acoustical Society of America*, vol. 120, Nov. 2006, pp. 2615–2626.

[13] Abdi A. and H. Guo, "Signal correlation modeling in acoustic vector sensor arrays," *IEEE Transactions on Signal Processing*, vol. 57, Mar. 2009, pp. 892–903.

[14] Radosevic A., J. G. Proakis, M. Stojanovic, "Statistical characterization and capacity of shallow water acoustic channels," *MTS/IEEE Proceedings of OCEANS'09-EUROPE*, Bremen, Germany, May. 2009, pp. 1-8.

[15] Zajić A. G., "Statistical space-time-frequency characterization of MIMO shallow water acoutsic channels," *MTS/IEEE Proceedings of OCEANS'09*, Biloxi, MS, Oct. 2009, pp. 1-6.

[16] Zajić A. G., "Statistical modeling of underwater wireless channels," *IEEE Proceedings of Global Telecommunications Conference, GLOBECOM'10*, Miami, FL, Dec. 2010, pp. 1–5.

[17] Zajić A. G., "Statistical modeling of MIMO mobile-to-mobile underwater channels," *IEEE Transactions on Vehicular Technology*, vol. 60, April 2011, pp. 1337–1351.

[18] Jakes W. C., *Microwave Mobile Communications*, 2nd ed. Piscataway, NJ: Wiley-IEEE Press, 1994.

[19] Stüber, G. L., *Principles of mobile communication*, 2nd ed. Norwell, MA: Kluwer, 2001.

[20] Zajić A. G., G. L. Stüber, T. G. Pratt, and S. Nguyen, "Wideband MIMO mobile-to-mobile channels: geometry-based statistical modeling with experimental verification," *IEEE Transactions on Vehicular Technology*, vol. 58, Feb. 2009, pp. 517-534.

[21] Yang T. C., "A study of spatial processing gain in underwater acoustic communications," *IEEE Journal of Oceanic Engineering*, vol. 32, July 2007, pp. 689–709.

[22] Yang T. C., "Toward continuous underwater acoustic communications," *MTS/IEEE Proceedings of OCEANS'08*, Quebec City, Canada, Sept. 2008, pp. 1–6.

[23] Gradshteyn I. S. and I. M. Ryzhik, *Table of Integrals, Series, and Products* , San Diego, CA, 5th ed., 1994.

[24] Pätzold M., U. Killat, and F. Laue, "An extended Suzuki model for land mobile satellite channels and its statistical properties," *IEEE Transactions on Vehicular Technology*, vol. 47, May 1998, pp. 617–630.

[25] Greenstein L. J., D. G. Michelson, and V. Erceg, "Moment-method estimation of the Ricean K-factor," *IEEE Communication Letters*, vol. 3, June 1999, pp. 175–176.

[26] A. Abdi, H. Zhang, and C. Tepedelenlioglu, "A unified approach to the performance analysis of speed estimation techniques in mobile communication," *IEEE Transactions on Communications*, vol. 56, Jan. 2008, pp. 126–135.

[27] B. Blankenagel and A. G. Zajić, "Simulation model for wideband mobile-to-mobile underwater fading channels," Proc. of IEEE VTC Spring'13, pp.1-5, Dresden, Germany, June 2013.

[28] B. Blankenagel and A. G. Zajić, "Envelope level crossing rate in mobile-to-mobile underwater fading channels," Proc. of IEEE ICC'13, pp. 1-5, Budapest, Hungary, June 2013.